Mon. Not. R. Astron. Soc. **387,** 577–600 (2008) doi:10.1111/j.1365-2966.2008.13280.x

Mass, metal, and energy feedback in cosmological simulations

Benjamin D. Oppenheimer[1]★ and Romeel Davé

[1]*Astronomy Department, University of Arizona, Tucson, AZ 85721, USA*

Accepted 2008 March 30. Received 2008 March 25; in original form 2007 December 11

ABSTRACT

Using GADGET-2 cosmological hydrodynamic simulations including an observationally constrained model for galactic outflows, we investigate how feedback from star formation distributes mass, metals, and energy on cosmic scales from $z = 6 \rightarrow 0$. We include instantaneous enrichment from Type II supernovae (SNe), as well as delayed enrichment from Type Ia SNe and stellar [asymptotic giant branch (AGB)] mass loss, and we individually track carbon, oxygen, silicon and iron using the latest yields. Following on the success of the momentum-driven wind scalings, we improve our implementation by using an on-the-fly galaxy finder to derive wind properties based on host galaxy masses. By tracking wind particles in a suite of simulations, we find: (1) wind material re-accretes on to a galaxy (usually the same one it left) on a *recycling time-scale* that varies inversely with galaxy mass (e.g. <1 Gyr for L^* galaxies at $z = 0$). Hence, metals driven into the intergalactic medium by galactic superwinds cannot be assumed to leave their galaxy forever. Wind material is typically recycled several times; the median number of ejections for a given wind particle is 3, so by $z = 0$ the total mass ejected in winds exceeds $0.5\Omega_{\rm b}$. (2) The physical distance winds travel is fairly independent of redshift and galaxy mass (∼60–100 physical kpc, with a mild increase to lower masses and redshifts). For sizeable galaxies at later epochs, winds typically do not escape the galaxy halo, and rain back down in a *halo fountain*. High-z galaxies enrich a significantly larger comoving volume of the intergalactic medium (IGM), with metals migrating back into galaxies to lower z. (3) The stellar mass of the typical galaxy responsible for every form of feedback (mass, metal, and energy) grows by ∼30 times between $z = 6 \rightarrow 2$, but only approximately two to three times between $z = 2 \rightarrow 0$, and is around or below L^* at all epochs. (4) The energy imparted into winds scales with $M_{\rm gal}^{1/3}$, and is roughly half the SN energy. Given radiative losses, energy from another source (such as photons from young stars) may be required to distribute cosmic metals as observed. (5) The production of all four metals tracked is globally dominated by Type II SNe at all epochs. However, intracluster gas iron content triples as a result of non-Type II sources, and the low-z IGM carbon content is boosted significantly by AGB feedback. This is mostly because gas is returned into the interstellar medium to form one-third more stars by $z = 0$, appreciably enhancing cosmic star formation at $z \lesssim 1$.

Key words: methods: numerical – galaxies: abundances – galaxies: evolution – galaxies: high-redshift – intergalactic medium – cosmology: theory.

1 INTRODUCTION

Galactic-scale feedback appears to play a central role in the evolution of galaxies and the intergalactic medium (IGM) over the history of the Universe. Mass feedback in the form of galactic outflows curtails star formation (SF) (e.g. Springel & Hernquist 2003b, hereafter SH03b) by removing baryons from sites of SF, thereby solving the overcooling problem where too many baryons condense into stars (e.g. Balogh et al. 2001). The energy in these winds carries metal-enriched galactic interstellar medium (ISM) gas out to large distances, where the metals are observed in quasar-absorption line spectra tracing the IGM (e.g. Cowie & Songaila 1998). Galactic outflows appear to be the only viable method to enrich the IGM to the observed levels as simulations show that tidal stripping only is not sufficient (Aguirre et al. 2001; Oppenheimer & Davé 2006, hereafter OD06). Hence, understanding galactic outflows is a key requirement for developing a complete picture of how baryons in all cosmic phases evolve over time.

Modelling galactic outflows in a cosmological context has now become possible, thanks to increasingly sophisticated algorithms and improving computational power. The detailed physics in

★E-mail: oppen@as.arizona.edu

© 2008 The Authors. Journal compilation © 2008 RAS

Downloaded from https://academic.oup.com/mnras/article/387/2/577/1022513 by guest on 16 August 2022

distributing the feedback energy from supernovae (SNe) and massive stars to surrounding gas still remains far below the resolution limit in such simulations, so must be incorporated heuristically. There are two varieties of approaches of feedback: thermal and kinetic. Kobayashi (2004) injects energy from galactic superwinds and SNe thermally into a number of surrounding gas particles in a smoothed particle hydrodynamic (SPH) simulation, and find that hypernovae with 10 times the typical SN energy are needed to enrich the IGM to observed levels while matching the stellar baryonic content of the local Universe (Kobayashi, Springel & White 2007). Springel & Hernquist (2003a) (hereafter SH03a) introduced kinetic feedback in SPH cosmological simulations where individual gas particles are given a velocity kick and their hydrodynamic forces are shut off for a period of 30 Myr or until they reach one-tenth the SF density threshold. By converting all the energy from SNe into kinetic outflows with constant velocity, SH03b are able to match the SF history of the Universe while enriching the IGM. Cen & Ostriker (2006) introduce a kinetic wind model in grid-based hydrodynamic simulations, and are able to match the observed IGM O VI lines in the local Universe (Cen & Fang 2006).

In OD06 we took the approach of scaling outflow properties with galaxy properties, and explored a variety of wind models winds in GADGET-2 simulations. We found that the scalings predicted by momentum-driven galactic superwinds (e.g. Murray, Quatert & Thompson 2005, hereafter MQT05) provide the best fit to a variety of quasar absorption line observations in the IGM, while also reproducing the observed cosmic SF history between $z = 6 \rightarrow 1.5$. In the momentum-driven wind scenario, radiation pressure from ultraviolet (UV) photons generated by massive stars accelerates dust, which is collisionally coupled to the gas, thereby driving galactic-scale winds. MQT05 formulated the analytical dependence of momentum-driven winds on the velocity dispersion of a galaxy, σ, deriving the relations for wind velocity, $v_{\rm wind} \propto \sigma$, and the mass loading factor 'i.e. the mass-loss rate in winds relative to the SF rate (SFR)', $\eta \propto \sigma^{-1}$. Observations by Martin (2005a) and Rupke, Veilleux & Sanders (2005) indicate that $v_{\rm wind}$ is proportional to circular velocity (where $v_{\rm circ} \sim \sigma$) over a wide range of galaxies ranging from dwarf starbursts to ultraluminous infrared galaxies. Mass outflow rates are difficult to measure owing to the multiphase nature of galactic outflows (Strickland et al. 2002; Martin 2005b), but at least at high z there are suggestions that the mass outflow rate is of the order of theSFR in Lyman break galaxies (LBGs) (Erb et al. 2006). A theoretical advantage of momentum-driven winds is that they do not have the same energy budget limitations as do SN energy-driven winds, where the maximum is $\sim 10^{51}$ erg per SN, because the UV photon energy generated over the main-sequence lifetime of massive stars is $\sim$100 times greater (Schaerer 2003). OD06 found that transforming all SN energy into kinetic wind energy often is not enough to drive the required winds, particularly at lower redshifts. Moreover, galactic-scale simulations find that in practice only a small fraction of SN energy is transferred to galactic-scale winds (Mac Low & Ferrara 1999; Fujita et al. 2004, 2008; Spitoni, Recchi & Matteucci 2008). In short, the momentum-driven wind scenario seems to match observations of large-scale enrichment, is broadly consistent with available direct observations of outflows, and relieves some tension regarding wind energetics.

Still, for the purposes of studying the cosmic metal distribution, the exact nature of the wind-driving mechanism is not relevant; in our models, what is relevant is how the wind properties scale with properties of the host galaxy. The inverse σ dependence of the mass loading factor appears to be necessary to sufficiently curtail SF in high-z galaxies (Davé, Finlator & Oppenheimer 2006; Finlator, Davé & Oppenheimer 2007). At the same time, they enrich the IGM to the observed levels through moderate wind velocities that do not overheat the IGM (OD06). Continual enrichment via momentum-driven wind scalings reproduces the relative constancy of Ω(C IV) from $z \approx 6 \rightarrow 1.5$ (OD06) and the approximate amount of metals in the various baryonic phases at all redshifts (Davé & Oppenheimer 2007, hereafter DO07). The observed slope, amplitude, and scatter of the galaxy mass–metallicity relation at $z = 2$ (Erb et al. 2006) is reproduced by momentum-driven wind scalings (Finlator & Davé 2008). While only a modest range of outflow models were explored in OD06, the success of a single set of outflow scalings for matching a broad range of observations is compelling. This suggests that simulations implementing these scalings approximately capture the correct cosmic distribution of metals. Hence, such simulations can be employed to study an important question that has not previously been explored in cosmological simulations: *How do outflows distribute mass, metals, and energy on cosmic scales?*

In this paper, we explore mass, metallicity, and energy feedback from SF-driven galactic outflows over cosmic time. We use an improved version of the cosmological hydrodynamic code GADGET-2 (Springel 2005) employing momentum-driven wind scaling relations, with two major improvements over what was used in OD06: (1) a more sophisticated metallicity yield model tracking individual metal species from Type II SNe, Type Ia SNe, and asymptotic giant branch (AGB) stars; and (2) an on-the-fly galaxy finder to derive momentum-driven wind parameters based directly on a galaxy properties. The OD06 simulations only tracked one metallicity variable from one source, Type II SNe, and used the local gravitational potential as a proxy for σ in order to determine outflow parameters. These approximations turn out to be reasonable down to $z \sim 2$, but at lower redshifts they become increasingly inaccurate; this was the primary reason why most of our previous work focused on $z \gtrsim 1.5$ IGM and galaxy properties. By low z, Type Ia SNe and AGB stars contribute significantly to cosmic enrichment (Wallerstein & Knapp 1998; Mannucci et al. 2005), and these sources have yields that depend on metallicity (Woosley & Weaver 1995; Limongi & Chieffi 2005). Our new simulations account for these contributions. Next, using the gravitational potential wrongly estimates σ especially at low z, when galaxies more often live in groups and clusters and the locally computed potential does not reflect the galaxy properties alone (as assumed in MQT05). This tends to overestimate $v_{\rm wind}$ and underestimate η, resulting in unphysically large wind speeds and insufficient suppression of SF at low redshifts. Our new simulations identify individual galaxies during the simulation run, hence allowing wind properties to be derived in a manner more closely following MQT05.

This paper progresses as follows. In Section 2, we describe in detail our modifications to GADGET-2, emphasizing the use of observables in determining our outflow prescription and metallicity modifications. Section 3 examines the energy balance from momentum-driven feedback between galaxies and the IGM using the new group finder-derived winds. We follow the metallicity budget over the history of the Universe in Section 4 first by source (Section 4.1), and then by location (Section 4.2), briefly comparing our simulations to observables including C IV in the IGM and the iron content of the intracluster medium (ICM). Section 5.1 examines the three forms of feedback (mass, metallicity, and energy) as a function of galaxy baryonic mass. We determine the typical galaxy mass dominating each type of feedback (Section 5.2). We then consider the cycle of material between galaxies and the IGM, introducing the key concept of *wind recycling* (Section 5.3) to differentiate between outflows that leave a galaxy reaching the IGM and *halo fountains* –

Downloaded from https://academic.oup.com/mnras/article/387/2/577/1022513 by guest on 16 August 2022

winds that never leave a galactic halo. We examine wind recycling as a function of galaxy mass in Section 5.4. Section 6 summarizes our results. We use Anders & Grevesse (1989) for solar abundances throughout; although newer references exist, these abundances are more easily comparable to previous works in the literature, and we leave the reader to scale the abundances to their favoured values.

2 SIMULATIONS

We employ a modified version of the *N*-body+hydrodynamic code GADGET-2, which uses a tree-particle-mesh algorithm to compute gravitational forces on a set of particles, and an entropy-conserving formulation of SPH (Springel & Hernquist 2002) to simulate pressure forces and shocks in the baryonic gaseous particles. This Lagrangian code is fully adaptive in space and time, allowing simulations with a large dynamic range necessary to study both high-density regions harbouring galaxies and the low-density IGM.

GADGET-2 also includes physical processes involved in the formation and evolution of galaxies. Star-forming gas particles have a subgrid recipe containing cold clouds embedded in a warm ionized medium to simulate the processes of evaporation and condensation seen in our own Galaxy (McKee & Ostriker 1977). Feedback of mass, energy, and metals from Type II SNe is returned to a gas particle's warm ISM at every time-step it satisfies the SF density threshold. In other words, gas particles that are *eligible* for SF undergo instantaneous self-enrichment from Type II SNe. The instantaneous recycling approximation of Type II SN energy to the warm ISM phase self-regulates SF resulting in convergence in SFRs when looking at higher resolutions (SH03a).

SF below $10\,\mathrm{M}_\odot$ is decoupled from their high-mass counterparts using a Monte Carlo algorithm that spawns star particles. In GADGET-2, a star particle is an adjustable fraction of the mass of a gas particle; we set this fraction to 1/2 meaning that each gas particle can spawn two star particles. The metallicity of a star particle remains fixed once formed; however, since Type II SNe enrichment is continuous while stars are formed stochastically, every star particle invariably has a non-zero metallicity. The total SFR is scaled to fit the disc surface density SFR observed by Kennicutt (1998), where a single free parameter, the SF time-scale, is set to 2 Gyr for a Salpeter (1955) initial mass function (IMF) (SH03a).

Even with self-regulation via the subgrid two-phase ISM, global SFRs were found to be too high, meaning another form of SF regulation is required. SH03b added galactic-scale feedback in the form of kinetic energy added to gas particles at a proportion relative to their SFRs. They set the wind energy equal to the Type II SN energy, thereby curtailing the SF in order to broadly match the observed global cosmic SF history. SH03b assumed a constant mass loading factor for the winds, which resulted in a constant wind velocity of $484\,\mathrm{km\,s^{-1}}$ emanating from all galaxies. OD06 found that scaling the velocities and mass-loading factors as prescribed by the momentum-driven wind model did a better job of enriching the high-z IGM as observed, while better matching the cosmic SF history.

We have performed a number of modifications to GADGET-2 since OD06. These include (1) the tracking of individual metal species, (2) metallicity-dependent SN yields, (3) energy and metallicity feedback from Type Ia SNe, (4) metallicity and mass feedback from AGB stars at delayed times, (5) a particle group finder to identify galaxies in situ with GADGET-2 runs so that wind properties can depend on their parent galaxies, and (6) a slightly modified implementation of momentum-driven winds. We describe each in turn in the upcoming subsections.

All simulations used here are run with cosmological parameters consistent with the three-year *WMAP* results (Spergel et al. 2007). The parameters are $\Omega_0 = 0.30, \Omega_\Lambda = 0.70, \Omega_\mathrm{b} = 0.048$, $H_0 = 69\,\mathrm{km\,s^{-1}\,Mpc^{-1}}, \sigma_8 = 0.83$, and $n = 0.95$; we refer to this as the *l*-series. Note that σ_8 is somewhat higher than the *WMAP3*-favoured value of 0.75, owing to observations suggesting that it may be as high as 0.9 (e.g. Rozo et al. 2007; Evrard et al. 2008). Our general naming convention, similar to OD06, is l(*boxsize*)n(*particles*/*side*)vzw-(*suffix*) where *boxsize* is in h^{-1} Mpc and the *suffix* specifies how the winds are derived ('σ' from the on-the-fly group finder, or 'Φ' from the local gravitational potential) and whether AGB feedback was *not* included ('nagb').

Table 1 lists parameters for our runs presented in this paper. We ran a series of test simulations with 2×128^3 particles in 8 and $32\,h^{-1}$ Mpc boxes to explore the effect of turning off the AGB

Table 1. Simulation parameters.

Name[a]	L[b]	ϵ[c]	m_SPH[d]	m_dark[d]	$M_\mathrm{gal,min}$[d,e]	z_end	AGB feedback?	Wind derivation
Test simulations								
l8n128vzw-Φ	8	1.25	4.72	29.5	151	0.0	Y	Φ
l8n128vzw-σ	8	1.25	4.72	29.5	151	0.0	Y	σ
l8n128vzw-σ-nagb	8	1.25	4.72	29.5	151	0.0	N	σ
l32n128vzw-Φ	32	5.0	302	1890	9660	0.0	Y	Φ
l32n128vzw-σ	32	5.0	302	1890	9660	0.0	Y	σ
l32n128vzw-σ-nagb	32	5.0	302	1890	9660	0.0	N	σ
High-resolution simulations								
l8n256vzw-σ	8	0.625	0.590	3.69	18.8	3.0	Y	σ
l16n256vzw-σ	16	1.25	4.72	29.5	151	1.5	Y	σ
l32n256vzw-σ	32	2.5	37.7	236	1210	0.0	Y	σ
l64n256vzw-σ	64	5.0	302	1890	9660	0.0	Y	σ
l64n256vzw-σ-nagb	64	5.0	302	1890	9660	0.0	N	σ

[a]The 'vzw' suffix refers to the momentum-driven winds with L_f varying between 1.05 and 2.0, metallicity-dependent v_wind, and an extra kick to get out of the potential.
[b]Box length of cubic volume, in comoving h^{-1} Mpc.
[c]Equivalent Plummer gravitational softening length, in comoving h^{-1} kpc.
[d]All masses quoted in units of $10^6\,\mathrm{M}_\odot$.
[e]Minimum resolved galaxy stellar mass.

Downloaded from https://academic.oup.com/mnras/article/387/2/577/1022513 by guest on 16 August 2022

feedback and using the old prescription of using potential-derived $v_{\rm wind}$. The 2×256^3 simulations are our high-resolution simulations and range in gas particle mass from 0.59×10^6 to $302 \times 10^6\,{\rm M}_\odot$. The l32n256vzw-$\sigma$ simulation was by far the most computationally expensive simulation taking in excess of 50 000 CPU hours on an SGI Altix machine. The l16n256vzw-σ simulation contains the minimum resolution needed to resolve C IV IGM absorbers (OD06); however, it is prohibitively expensive to run this to $z = 0$. We will use the l8n128vzw simulations at the same resolution but a smaller box to explore these absorbers; this box appears to converge with the l16n256vzw simulation at $z = 1.5$, despite containing a smaller volume unable to build larger structures.

2.1 Metal yields

In previous GADGET-2 simulations including SH03b and OD06, metal enrichment was tracked with only one variable per SPH particle representing the sum of all metals and was assumed to arise from only one source, Type II SNe, which enriched instantaneously. While this is reasonably accurate when considering oxygen abundances, the abundances of other species can be significantly affected by alternate sources of metals.

We have implemented a new yield model that tracks four species (carbon, oxygen, silicon and iron) from three sources (Type II SNe, Type Ia SNe, and AGB stars) all with metallicity-dependent yields. These sources have quite different yields that depend significantly on metallicity, and inject their metals at different times accompanied by a large range in energy feedback. A more sophisticated yield model is required to model metal production from the earliest stars, abundance variations within and among galaxies, abundance gradients within the IGM, and abundances in the ICM.

The four species chosen not only make up 78 per cent of all metals in the sun (Anders & Grevesse 1989), but are also the species most often observed in quasar absorption line spectra probing the IGM, X-ray spectra of the ICM, and the ISM of galaxies used to determine the galaxy mass–metallicity relationship. Furthermore, because these metals are among the most abundant, they are also often the most dynamically important when considering metal production in stars, the multiphase ISM, and metal-line cooling of the IGM. We have not implemented metal-line cooling per individual species, but this may be straightforwardly incorporated in the future.

2.1.1 Type II SNe

Type II SN enrichment follows that presented in SH03a, namely their equation (40) where gas particles are self-enriched instantaneously via

$$\Delta Z_{\rm species} = (1 - f_{\rm SN}) y_{\rm species}(Z) x \frac{\delta t}{t_*}, \quad (1)$$

where $f_{\rm SN}$ is the fraction of the stellar IMF that goes SN, x is the fraction of an SPH gas particle in the cold ISM phase, and t_* is the SF time-scale. Our modification is that we follow the yield of each species individually using metallicity-dependent yields, $y_{\rm species}(Z)$, from the nucleosynthetic calculations by Limongi & Chieffi (2005) instead of assuming $y = {\rm Z}_\odot = 0.02$ as SH03b and OD06 did. Their grid of models include SNe ranging from 13 to $35\,{\rm M}_\odot$ and metallicities ranging from $Z = 0$ to 0.02. Using the total metallicity of a gas particle (i.e. the sum of the four species divided by 0.78 to account for other species), we employ a lookup table indexed by metallicity to obtain the $y_{\rm species}(Z)$. The Limongi & Chieffi (2005) yields are the most complete set of metallicity-dependent yields since Woosley & Weaver (1995). Both papers find similar yields for carbon and oxygen, the two species most important for IGM observations.

We use the Chabrier (2003) IMF, although it is quite possible to modify the IMF in the future so as to have a top-heavy IMF under different conditions (e.g. Davé 2008). We assume that all stars between 10 and $100\,{\rm M}_\odot$ go SN, comprising $f_{\rm SN} = 0.198$ (i.e. 19.8 per cent of the total stellar mass in the IMF). We use the yields of Limongi & Chieffi (2005) comprising 13–35 $\rm M_\odot$ over this larger mass range, thus assuming the similar yields from stars between 10–13 and 35–$100\,{\rm M}_\odot$. Other SN yield models that include more massive stars (Portinari, Chiosi & Bressan 1998; Hirschi, Meynet & Maeder 2005) show higher carbon and oxygen yields from stars over $40\,{\rm M}_\odot$ at solar metallicity, but do not cover the range of metallicities of Limongi & Chieffi (2005). The fraction of stars going SN, $f_{\rm SN}$, is nearly twice as high since SH03a assumes a Salpeter IMF ($f_{\rm SN} = 0.1$), because there is a turnover at masses less than $1\,{\rm M}_\odot$. The remaining 80.2 per cent form star particles from which AGB feedback arises at later times.

2.1.2 Type Ia SNe

Type Ia SNe are believed to arise from mass accretion from a companion star that increases the mass beyond the Chandrasekhar limit, causing an explosion. Recently, the Type Ia SN rate was measured by Mannucci et al. (2005), and the resulting data were parametrized by Scannapieco & Bildsten (2005) with a two-component model, where one component is proportional to the stellar mass ('slow' component), and the other to the SFR ('rapid' component):

$${\rm SNR_{Ia}} = A M_\star + B \dot{M}_\star \quad {\rm M_\odot\,yr^{-1}}. \quad (2)$$

Scannapieco & Bildsten (2005) determined that the best fit to the Mannucci et al. (2005) data was provided by $A = 4.4 \times 10^{-14}\,{\rm yr}^{-1}$ and $B = 2.6 \times 10^{-3}$, with a time-delay of 0.7 Gyr in the slow component for the onset of Type Ia SN production.

To implement this in GADGET-2, we calculate the number of Type Ia SNe formed at each time-step for every gas particle (from the first part of equation 2) and every star particle where the star was formed more than 0.7 Gyr ago (from the second term in equation 2). Each Type Ia SN is assumed to add 10^{51} erg of energy, which is added directly to the gas particle or, in the case of star particles, added to the nearest gas particle. Each Type Ia SN is also assumed to produce $0.05\,{\rm M}_\odot$ of carbon, $0.143\,{\rm M}_\odot$ of oxygen, $0.150\,{\rm M}_\odot$ of silicon, and $0.613\,{\rm M}_\odot$ of iron with these four species making up 78 per cent of all metals made of Type Ia SNe (Thielemann, Nomoto & Yokoi 1986; Tsujimoto et al. 1995).

2.1.3 AGB stars

Feedback from AGB stars comprise at least half of the total mass returned to the ISM (Wallerstein & Knapp 1998). AGB stars copiously produce carbon, referred to as carbon stars, and other isotopes of carbon, nitrogen, and oxygen (Renzini & Voli 1981) on a delayed time-scale compared to the relatively instantaneous enrichment of Type II SNe. Heavier elements such as silicon and iron that remain unprocessed by low-mass stars can now be returned back into the ISM instead of being trapped in stars. The mass and metallicity feedback from AGB stars is considerable and in some regions even dominant over SNe. However, relative to SNe, the energy feedback can be considered negligible, since most of the mass leaves AGB stars at far less than $100\,{\rm km\,s^{-1}}$.

Downloaded from https://academic.oup.com/mnras/article/387/2/577/1022513 by guest on 16 August 2022

First, we consider the mass feedback as a function of time for a star particle. We use the Bruzual & Charlot (2003) stellar synthesis models using the Padova (1994) (Bressan et al. 1993) libraries of stellar evolution tracks to determine the mass-loss rate from non-SN stars as a function of age, given a Chabrier IMF. Mass-loss rates are calculated at an age resolution of 0.02 dex for six different metallicities ($Z = 0.0001$, 0.0004, 0.004, 0.008, 0.02 and 0.05) covering stellar ages from $\log(t) = 7.18$ to 10.14 (i.e. the age of the death of the most-massive AGB stars to the age of the Universe). We interpolate in age and metallicity.

To implement this in GADGET-2, we use each star particle's age and metallicity to determine the mass-loss rate from a lookup table generated from the Bruzual & Charlot (2003) population synthesis models. This is performed for every star particle each time-step with the total amount of mass lost being the product of the time-step and the mass-loss rate. This mass is then transferred to the three nearest gas particle neighbours using a neighbour search.

To illustrate the importance of mass feedback from low-mass stars, consider a stellar population at $Z = 0.02$, which by $\log(t) = 7.34$ yr has returned about 17.5 per cent of its mass via SN feedback. By 100 Myr another 10.3 per cent of the mass is returned to the ISM, and another 12.0 per cent is returned by 1 Gyr. More mass is returned to the ISM in the first Gyr from AGB stars than SNe. Another 9.7 per cent is returned between 1 and 10 Gyr. Overall, slightly greater than 50 per cent of the mass of a Chabrier IMF is returned to the ISM with more than 30 per cent coming from low and intermediate-mass stars.

To model the return of metals into the ISM, we use the stellar yield models of Herwig (2004) ($Z = 0.0001$), Marigo (2001) ($Z = 0.008$), and Gavilán, Buell & Mollá (2005) ($Z = 0.0126$, 0.0200, 0.0317) for a variety of stellar masses. We take the age at which a given stellar mass ends its life, from which we generate an interpolated lookup table of yields for a given species analogous to the mass-loss lookup table. The incremental parcel of mass lost during each time step for each star particle is given a yield corresponding to the mass of a star dying at the star particle's age. This assumes that only one specific stellar mass is contributing to the entire mass loss from a stellar population at a given age, which is not a bad assumption considering that intermediate-mass stars lose most of their mass during the short-lived AGB stage.

We calculate AGB yield lookup tables for carbon and oxygen only. Silicon and iron remain almost completely unprocessed in low- and intermediate-mass stars, so therefore we simply take their yields to be the original abundances of the star particle when it formed. To illustrate the yields, Fig. 1 plots the carbon yield as a function of age for a variety of metallicities. The dashed line is the relation between the zero-age main-sequence mass and the age of death. Carbon stars enrich copiously between ~200 Myr and 1 Gyr corresponding to stars of masses 2–4 $M_\odot$ going through the AGB stage. The reason for this is that third dredge-up becomes efficient above 2 $M_\odot$ transporting the products of double shell burning into the envelope (i.e. C^{12}) until hot-bottom burning becomes efficient above 4–5 $M_\odot$ transforming carbon into nitrogen. Lia, Portinari & Carraro (2002) also added delayed AGB feedback into SPH simulations, although they do not extract yields directly from models; instead they use a time-dependent yield function without metallicity dependence for carbon.

It is worth pointing out that our simulations do not track the metals in stellar remnants. The metal products arising from nucleosynthesis in AGB stars for the most part remain in the white dwarf remnant once it has blown its envelope off, and we do not track the creation of these metals in the star particles. The same is true for neutron stars and stellar black holes. Fortunately, these metals remain locked in their stellar remnants on time-scales far beyond the age of the Universe; hence, we can ignore them as a component of observable metals. When we talk about the global metal budgets in Section 4, we do not include metals trapped in stellar remnants.

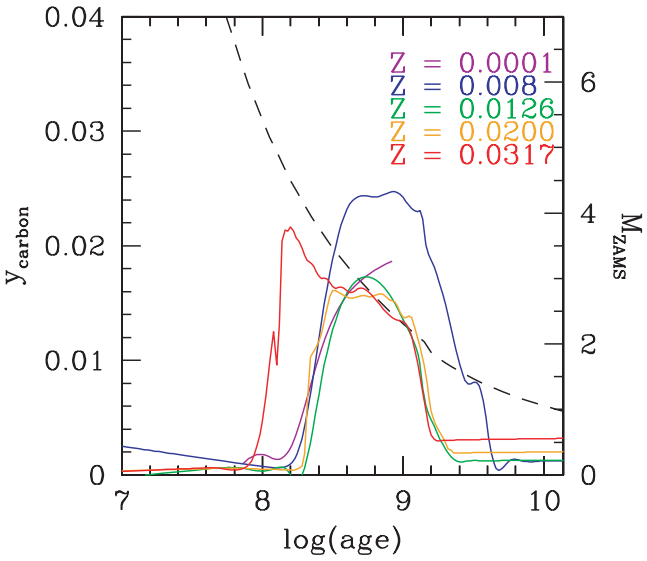

Figure 1. Carbon yields of gas lost from AGB stars for several metallicities calculated by Herwig (2004), Marigo (2001) and Gavilán et al. (2005) converted from a function of stellar mass to a function of age by using a star's lifetime (dashed line). In GADGET-2, we take a star particle's age and assign the yield from these curves to the fractional amount of mass lost from the star particle and added to the three nearest SPH neighbours. The carbon yields jump between ~200 Myr and 1 Gyr when AGB stars in the range of 2–4 $M_\odot$ are dying as carbon stars; AGB yields are highly dependent on age as well as metallicity. The $Z = 0.008$ yields show the strongest yields, especially towards lower mass, while by $Z = 0.0317$ the strongest yields come from 5-$M_\odot$ stars.

2.2 Group finder

A group finder added to GADGET-2 allows us to add new dynamics based on the properties of a gas or star particle's parent galaxy. This is especially important for momentum-driven winds, which MQT05 argued depend on the properties of a galaxy as a whole (specifically a galaxy's σ). We will show in Section 2.3 that winds derived from the group finder more accurately determine wind speeds for the momentum-driven wind model versus using the potential well depth of a particle as a proxy of galaxy mass as was done in OD06 and DO07.

Our group finder is based on the friends-of-friends (FOF) group finder kindly provided to us by V. Springel, which we modified and parallelized to run in situ with GADGET-2. Gas and star particles within a specified search radius are grouped together and cataloged if they are above a certain mass limit, which we set to be 16 gas particle masses. The search radius is set to 0.04 of the mean interparticle spacing corresponding to an overdensity of $(1/0.04)^3 = 15\,625$. We chose this value after numerous comparisons with the more sophisticated (but far more computationally expensive) Spline Kernel Interpolative DENMAX (SKID)[1] group finder performed on snapshot outputs.

[1] http://www-hpcc.astro.washington.edu/tools/skid.html.

© 2008 The Authors. Journal compilation © 2008 RAS, MNRAS **387,** 577–600

Downloaded from https://academic.oup.com/mnras/article/387/2/577/1022513 by guest on 16 August 2022

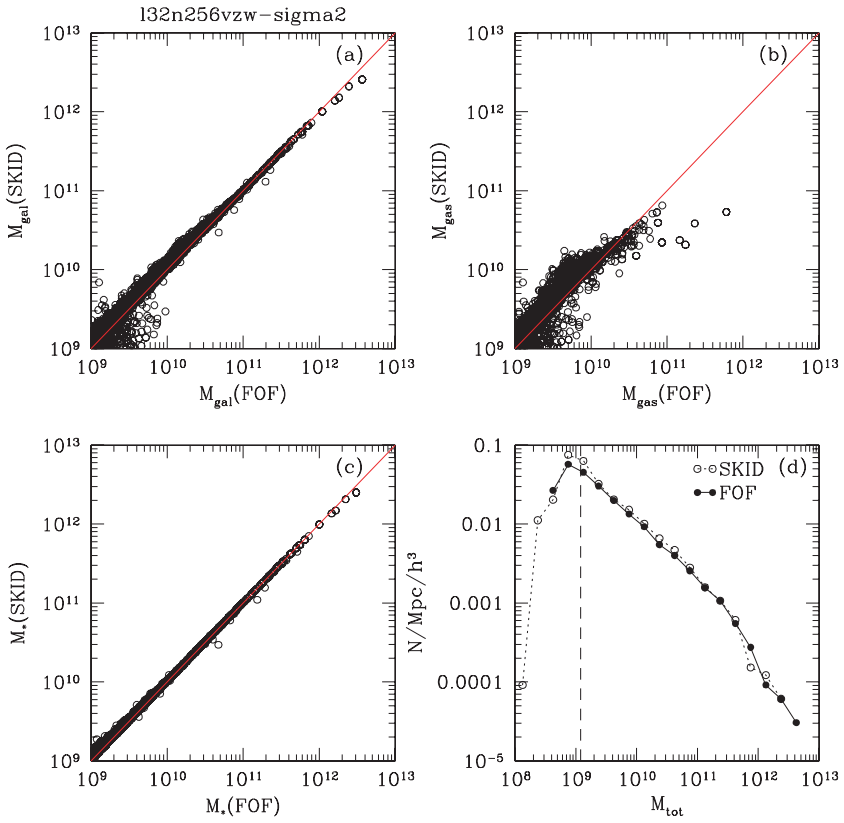

Figure 2. The comparison of two group finders run on a $32\,h^{-1}$ Mpc 2×256^3 simulation at $z = 0$. FOF is the much faster algorithm run in situ with GADGET-2 at frequent intervals to determine galaxy properties on the fly, while SKID is a post-processing DENMAX algorithm run on simulation snapshots. Panels (a), (b) and (c) compare the masses (total, gas and stellar mass, respectively) of groups found within 5 kpc of each other by the two group finders. Stellar masses agree very well while the gas masses (a smaller component by $z = 0$) show more scatter. The total mass functions (panel d) of both group finders lie nearly on top of each other above the resolution limit (dashed line), although FOF tends to group some satellites found by SKID with the largest few galaxies. The $M_{\rm gal}$ functions do not resemble a Schechter function, although when one plots M_* there is a more pronounced turnover below $M_* = 10^{10}\,{\rm M}_\odot$.

The FOF group finder is run every third domain decomposition, which corresponds to an interval usually between 2 and 10 Myr depending on the dynamical time-stepping for the given simulation (i.e. smaller time-steps for higher resolution). This time-step was chosen to be smaller than the dynamical time-scales of most if not all galaxies resolved in a particular simulation. The galaxy properties output include gas and stellar mass and metallicities, SFR, and fraction of gas undergoing SF. The additional CPU cost ranges from 7 to 10 per cent for a 64-processor run to less than 5 per cent for a 16-processor run. Once the FOF group finder is run, each particle in a galaxy is assigned an ID so that it can be easily linked to all the properties of its parent galaxy.

A comparison plot of the two group finders in Fig. 2 for the l32n256vzw-σ simulation at $z = 0$ shows very good but not perfect agreement for total baryonic galaxy mass ($M_{\rm gal}$, panel a). Galaxies are matched up by requiring a $<5\,h^{-1}$ kpc difference between SKID and FOF positions. Stellar masses (M_*, lower left-hand panel) are nearly identical, but the associated gas mass ($M_{\rm gas}$, upper right-hand panel) shows more scatter. Note that there is no explicit density or temperature threshold for including gas in the FOF case, but in the SKID case only gas with overdensities >1000 compared to the cosmic mean are included; this may contribute to some of the scatter. FOF group finders have the tendency to group too many things together in dense environments, and this is most notable in the associated gas masses. There are significantly better agreements in gas masses at higher redshift, where dense group/cluster environments are less common and gas fractions are greater.

The mass functions of both group finders when all galaxies are included show very good agreement (lower right-hand panel of Fig. 2). SKID and FOF each finds six galaxies with $M_{\rm gal} > 10^{12}\,{\rm M}_\odot$, 112 and 113 galaxies with $10^{12} > M_{\rm gal} > 10^{11}\,{\rm M}_\odot$, 793 and 719 galaxies with $10^{11} > M_{\rm gal} > 10^{10}\,{\rm M}_\odot$, and 4296 and 3596 galaxies with $10^{10} > M_{\rm gal} > 10^{9}\,{\rm M}_\odot$, respectively. $1.2 \times 10^9\,{\rm M}_\odot$ is the galaxy mass resolution limit defined as the mass of 64 SPH particles (Finlator et al. 2006). Owing to the tendency of FOF to over group satellite galaxies with central galaxies in dense environments, there is a deficiency of small satellite galaxies in the FOF case. The total amount of mass in all resolved galaxies is within 0.2 per cent between the two group finders; however, there is 24 per cent more mass grouped to the six largest galaxies in the FOF finder.

As a side note, our group finder has the flexibility to enable modelling of merger-driven or mass-threshold processes such as active galactic nucleus (AGN) feedback. Although our simulations implicitly include both hot- and cold-mode accretion (Kereš et al. 2005), Dekel & Birnboim (2006) suggests that AGN feedback affects only hot-mode accretion, and hence there exists a threshold halo mass above which AGN feedback is effective. Our group finder can identify galaxies where AGN feedback may be necessary to curtail SF and drive AGN winds. Conversely, if AGN feedback is driven by the onset of a merger (Di Matteo, Springel & Hernquist 2005), our group

Downloaded from https://academic.oup.com/mnras/article/387/2/577/1022513 by guest on 16 August 2022

finder can identify mergers and add merger-driven AGN feedback that curtails SF. We leave such implementations of AGN feedback for future work, though we note that the heating of gas may transport a non-trivial amount of energy and metals into the IGM.

Frequent outputs of the group finder allow us to track the formation history of galaxies to see how galaxies build their mass (e.g. through accretion or mergers). We can trace the SFR during individual mergers to see if our simulations are producing bursts of SF. Outputting group finder statistics during a run allows us to immediately look at integrated properties such as the galaxy mass function, the mass–metallicity relationship, and the specific SFR as a function of mass just to name a few. This is valuable as these relations may exhibit changes in time-scales shorter than the simulation snapshot output frequency.

2.3 Wind model modifications

We use the same kinetic wind implementation of SH03a, whereby particles enter the wind at a probability η, the mass loading factor relative to the SFR. Wind particles are given a velocity kick, $v_{\rm wind}$, in a direction given by $\boldsymbol{v} \times \boldsymbol{a}$ (ie. perpendicular to the disc in a disc galaxy). These particles are not allowed to interact hydrodynamically until either they reach a SPH density less than 10 per cent of the SF density threshold or the time it takes to travel 30 kpc at $v_{\rm wind}$; the first case overwhelms the instances of the second case in our simulations. We admit that this phenomenological wind implementation insufficiently accounts for the true physics of driving superwinds as well as the multiphase aspect of winds (Strickland et al. 2002; Martin 2005b); see Dalla Vecchia & Schaye (2008) for an in-depth discussion of some of the insufficiencies of such winds in simulations. However, we want to stress that while we cannot hope to model the complexities of the outflows, the focus of this paper primarily depends on the much longer period of subsequent evolution. We use the momentum-driven wind model with variable $v_{\rm wind}$ and η, due to its successes in previous publications mentioned earlier.

In the momentum-driven wind model analytically derived by MQT05, $v_{\rm wind}$ scales linearly with the galaxy velocity dispersion, σ, and η scales inversely linearly with σ. We again use the following relations:

$$v_{\rm wind} = 3\sigma\sqrt{f_{\rm L} - 1}, \tag{3}$$

$$\eta = \frac{\sigma_0}{\sigma}, \tag{4}$$

where $f_{\rm L}$ is the luminosity factor in units of the galactic Eddington luminosity (i.e. the critical luminosity necessary to expel gas from the galaxy), and σ_0 is the normalization of the mass loading factor. The outflow models used in this paper are all of the 'vzw' variety described in Section 2.4 of OD06, in which we randomly select luminosity factors between $f_{\rm L} = 1.05$ and 2.00, include a metallicity dependence for $f_{\rm L}$ owing to more UV photons output by lower metallicity stellar populations

$$f_{\rm L} = f_{\rm L,\odot} \times 10^{-0.0029(\log Z + 9)^{2.5} + 0.417\,694}, \tag{5}$$

and add an extra kick to get out of the potential of the galaxy in order to simulate continuous pumping of gas until it is well into the galactic halo (as argued by MQT05).

One difference is that we use $\sigma_0 = 150\,{\rm km\,s^{-1}}$ instead of $300\,{\rm km\,s^{-1}}$ in the equation for $\eta = \sigma_0/\sigma \times$ SFR. Since our assumed *WMAP3* cosmology produces less early structure than the *WMAP1* cosmology used in OD06, it requires less suppression of early SF and hence lower mass loading factors (DO07). We find that $\sigma_0 = 150\,{\rm km\,s^{-1}}$ with the *WMAP3* cosmology generally reproduces the success of $\sigma_0 = 300\,{\rm km\,s^{-1}}$ with the *WMAP1* cosmology.

The main modification we make to the outflow implementation is how σ is derived. Putting the wind parameters in terms of σ is the most natural, because the fundamental quantity MQT05 use to derive momentum-driven winds is $\sqrt{\frac{GM}{r}}$, which equals $\sqrt{2}\sigma$ for an isothermal sphere. In previous runs without a group finder, we derived σ using the virial theorem where $\sigma = \sqrt{-\frac{1}{2}\Phi}$, with Φ being the gravitational potential at the initial launch position of the wind particle. We will call this old form of the wind model Φ-derived winds. While this derivation of σ should adequately work for an isothermal sphere, the Φ calculated by GADGET-2 is the entire potential: the galaxy potential on top of any group/cluster potential. As galaxies live in groups and clusters more often low redshift, the wind speeds from Φ-derived winds become overestimated. To counteract this trend, we artificially implemented a limit of $\sigma = 266\,{\rm km\,s^{-1}}$, which corresponds to a $M_{\rm gal} \sim 2.7 \times 10^{12}\,{\rm M_\odot}$, the mass of a giant elliptical galaxy at $z = 0$. In the deep potential of a cluster, all galaxies no matter what size would drive winds at the speed of this upper limit. The overestimate of $v_{\rm wind}$ prevented us from trusting our wind model at lower redshifts; therefore, we usually stopped our simulations in OD06 at $z = 1.5$.

We now introduce σ-derived winds, where σ is calculated from $M_{\rm gal}$ as determined by the group finder. We use the same relation as MQT05 (their equation 6) from Mo, Mau & White (1998) assuming the virial theorem for an isothermal sphere:

$$\sigma = 200\left[\frac{M_{\rm gal}}{5\times10^{12}}\frac{\Omega_{\rm m}}{\Omega_{\rm b}}h\frac{H(z)}{H_0}\right]^{1/3}\,{\rm km\,s^{-1}}. \tag{6}$$

Since our group finder links only baryonic mass, we multiply $M_{\rm gal}$ by $\Omega_{\rm m}/\Omega_{\rm b}$ to convert to a dynamical mass. The wind properties are hence estimated from the galaxy alone. We do not calculate σ from the velocity dispersion of star and/or gas particles in the galaxy, since our tests show that the resolution is insufficient to derive a meaningful σ.

The $H(z)/H_0$ factor in equation (6) increases σ for a given mass as $H(z)$ increases at higher redshift. For example, $H(z=6) = 10.2 \times H_0$ resulting in winds being 2.17 times as fast being driven from the same mass galaxy at $z = 6$ versus $z = 0$. Physically, galaxies that form out of density perturbations at higher z have overcome faster Hubble expansion, and therefore their σ is higher. The same mass galaxy formed at higher redshift with a higher σ means the higher redshift galaxy must be more compact. Such a scenario is supported by the observations by Trujillo et al. (2006) and Trujillo et al. (2007) showing a trend of galaxies becoming smaller from $z = 0 \rightarrow 2$, in general agreement with Mo et al. (1998). A more compact galaxy drives a faster wind in the momentum-driven wind model, because $v_{\rm wind}$ is a function of $M_{\rm gal}/r$, not just $M_{\rm gal}$; there is more UV photon flux impinging on each dust particle. We will show that increasing $v_{\rm wind}$ emanating from the same mass galaxy towards higher z has important consequences in enriching the IGM at high z while not overheating it at low z.

Another modification to the wind model we add are new $v_{\rm wind}$ speed limits. The first depends on the SF time-scale, $\tau_{\rm SFR}$. The momentum-driven wind equation derived by MQT05 and used in OD06 and DO07 assumes that a starburst occurs of the order of a dynamical time-scale, $\tau_{\rm D}$, which is often the case in a merger-driven starburst. However, MQT05 also derive a maximum σ, $\sigma_{\rm max}$, above which a starburst cannot achieve the luminosity needed to expel the gas in an optically thick case. Although it is not clear how

Downloaded from https://academic.oup.com/mnras/article/387/2/577/1022513 by guest on 16 August 2022

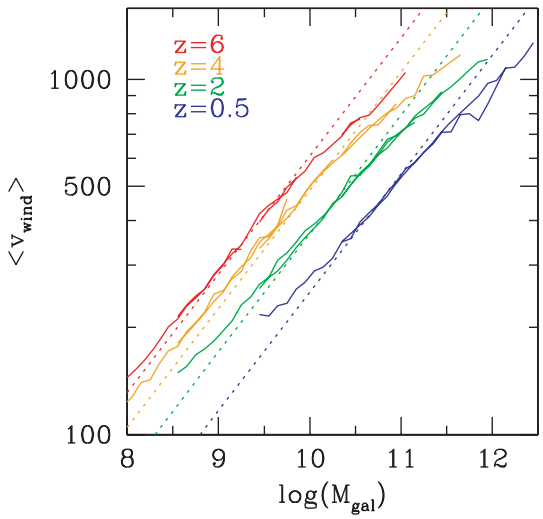

Figure 3. Average launch wind speed as a function of $M_{\rm gal}$ (derived using SKID) versus dotted lines for the predicted $\langle v_{\rm wind}\rangle$ assuming no speed limits. The wind speeds, which are derived using the FOF finder during a run, agree very well with the masses determined by SKID in the post-processing stage. The decline in $\langle v_{\rm wind}\rangle$ with redshift for a given $M_{\rm gal}$ is a result of the $H(z)$ dependence in equation (6). This trend loosely matches observations of faster winds for a given mass galaxy at high redshift.

$\sigma_{\rm max}$ varies with the $\tau_{\rm SFR}$, we modify their equation (23) to have an inverse linear dependence on the SF time-scale:

$$\sigma_{\rm max} = 4000 \times \frac{\tau_{\rm D}}{\tau_{\rm SFR}}\ {\rm km\,s^{-1}} \quad (7)$$

and assume a $\tau_{\rm D}$ of 50 Myr. The end result is a reduction of 5–10 per cent in the average $v_{\rm wind}$ out of $M_{\rm gal} \sim 10^{12}$ at $z < 1$.

A second speed limit we impose allows no more than two times the total SN energy to be deposited into the wind. This does not violate the energetics as the energy for these winds is coming from momentum deposition over the entire lifetime of a star, which is of the order of 100 times the SN energy (Schaerer 2003). This limit was instituted to disallow extreme values of $v_{\rm wind}$ (i.e. $>1500\,{\rm km\,s^{-1}}$) emanating from the most-massive haloes, reducing $v_{\rm wind}$ at most 30–50 per cent in the most-massive galaxies at $z < 1$.

In Fig. 3, we plot the average wind speed, $\langle v_{\rm wind}\rangle$, as a function of galaxy mass at four redshifts for a variety of box sizes ranging from 8 to $64\,h^{-1}$ Mpc along. The dotted lines show the predicted $\langle v_{\rm wind}\rangle$ for solar metallicity, assuming no speed limits. As with every plot in this paper, $M_{\rm gal}$ is the SKID-derived baryonic mass, not the FOF-derived mass from which $v_{\rm wind}$ is calculated. The simulations reproduce the predicted trend $v_{\rm wind} \propto M_{\rm gal}^{1/3}$. Divergences at low-mass result from faster winds being driven by low-mass, low-metallicity galaxies as well as some satellites being grouped with a central galaxy in groups/clusters by FOF. The latter effect appears to be subdominant though as evidenced by the overlap of the relation among simulations at different redshifts. The deviations at the high-mass end at all redshifts are dominated by the second wind speed limit discussed above.

The reduction in $v_{\rm wind}$ for a given mass galaxy due to the $H(z)$ dependence in equation (6) is the reverse of the trend in the Φ-derived models, and is in better agreement with low-z observations. In the new σ-derived wind model, a 10^{11}-$M_\odot$ galaxy (such as the Milky Way) launches an average wind particle at $790\,{\rm km\,s^{-1}}$ wind at $z = 3$ and $450\,{\rm km\,s^{-1}}$ at $z = 0$ while the corresponding values for the Φ-derived winds without any speed limits are 1040 and $1220\,{\rm km\,s^{-1}}$, respectively. The latter are far above the values observed in the local Universe. Martin (2005a) found that the relation $v_{\rm term} \propto 2.1\,v_{\rm circ}$ fits her observations best, where $v_{\rm term}$ is the terminal velocity of the wind. For a 10^{11}-$M_\odot$ galaxy, this corresponds to $v_{\rm circ} \sim 125\,{\rm km\,s^{-1}}$ leading to $v_{\rm term} \sim 265\,{\rm km\,s^{-1}}$. This is much nearer our σ-derived value once the extra velocity boost to leave the potential of the galaxy is subtracted. High-velocity clouds (HVCs) may be material that is blown into the halo from the Milky Way (Wakker & van Woerden 1997), and these have velocities that are $\ll 1000\,{\rm km\,s^{-1}}$, in better agreement with velocities expected in the σ-derived model. Of course, the Milky Way is not a starbursting galaxy driving a powerful wind; however, it is still possible that it is kicking up a significant amount of gas into the halo. Indeed, as we will discuss later (Section 5.4), the outflows in our simulations do not always reach the IGM, but particularly at low z may be more aptly described as 'halo fountains', where the outflows only propagate out to distances comparable to the galactic halo.

It remains very difficult to determine from observations whether wind speeds increase for a given mass galaxy at high z as the σ-derived winds predict. Observing asymmetric Lyman α profiles,Wilman et al. (2005) find what they interpret as $290\,{\rm km\,s^{-1}}$ outflows around an LBG with 10^{11}-$M_\odot$ baryons at $z = 3.09$. More recently Swinbank et al. (2007) observe outflows up to $500\,{\rm km\,s^{-1}}$ at $z = 4.88$ around a lensed galaxy with a dynamical mass as low as $10^{10}\,M_\odot$. These observed outflows appear to be beyond the virial radius in both cases and correspond to our velocities once we have subtracted the extra velocity boost we add to get out of the potential well. Our $v_{\rm term}$ for the Wilman et al. (2005) $z = 3$ galaxy would be closer to $500\,{\rm km\,s^{-1}}$, somewhat above their observed values. We expect $v_{\rm wind} \sim 300\,{\rm km\,s^{-1}}$ ($v_{\rm term} \sim 200\,{\rm km\,s^{-1}}$) for the Swinbank et al. (2007) object, but their mass is only a lower limit. If this object is a 10^{10}-$M_\odot$ baryonic-mass galaxy, we would derive $v_{\rm term} \sim 400\,{\rm km\,s^{-1}}$. Overall, the σ-derived winds predict velocities that are at least in the ballpark of observed values. Additionally, surveys of LBGs at $z \sim 3$ (Pettini et al. 2001; Shapley et al. 2003) find outflows of several hundred ${\rm km\,s^{-1}}$ to be ubiquitous, often driving an amount of mass comparable to the star-forming mass (i.e. $\eta \sim 1$)

3 THE UNIVERSAL ENERGY BALANCE

Armed with these new simulations, we can now investigate how outflows move mass, metals, and energy around the Universe. In this section, we focus on the energetics of outflows, and its impact on cosmic SF and temperature. We will compare the new σ-derived wind model's behaviour versus the old Φ-derived wind model, and study the impact of AGB feedback. Specifically, σ-derived winds inject much less energy at late times making a cooler and less-enriched IGM while leading to more SF. The inclusion of AGB feedback does not really affect the global energy balance, but does increase the number of stars formed and more significantly affects the amount and location of metals, as we discuss in Section 4.

The history of the cosmic SFR density (SFRD; Lilly et al. 1996; Madau et al. 1996) is a key observable that has received much attention in recent years (e.g. Hopkins & Beacom 2006; Fardal et al. 2007). The SFRD plot in the upper left-hand panel of Fig. 4 shows how our models compare to the Hopkins & Beacom (2006) compilation (black lines, two different fits). It should be noted that we are resolving galaxies down to $\approx 10^{10}\,M_\odot$ in the models shown with the solid lines, and hence the SF density at $z \gtrsim 3$ is increasingly underestimated (see e.g. SH03b). Hence, this should be considered as an illustrative comparison, whose main point is to highlight the differences between various models. A more complete SF history at

Downloaded from https://academic.oup.com/mnras/article/387/2/577/1022513 by guest on 16 August 2022

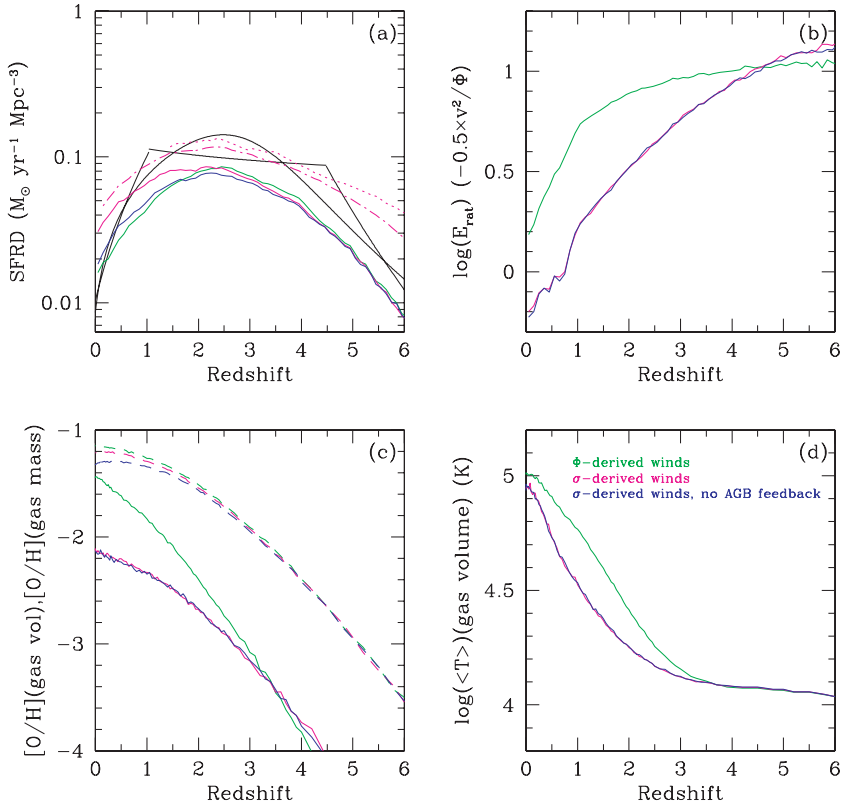

Figure 4. Three $32\,h^{-1}$ Mpc 2×128^3 simulations: Φ-derived winds including AGB feedback (green), σ-derived winds with AGB feedback (magenta), and σ-derived winds without AGB feedback (blue) demonstrate how global quantities evolve as a result of energetic interactions between SF-driven feedback from galaxies and the state of the IGM. Panel (a) shows the SF density histories compared to the Hopkins & Beacom (2006) compilation averages (black lines for segmented and non-segmented fit, scaled to a Chabrier IMF). Panel (b) shows the average virial ratio with which wind particles are launched. The solid/dashed lines in panel (c) trace the volume/mass-weighted average gas oxygen content, and panel (d) shows the volume-weighted temperature. The new σ-derived winds do not inject as much energy or metals into the IGM while increasing the SF. AGB feedback has a relatively minor effect in the energetic balance between galaxies and the IGM. The lower resolution l32n128 simulation misses about half of all SF; therefore, we also show the l32n256 (dash–dotted line) and the l16n256 (dotted line) simulations in panel (a), which both agree better with observations.

early times is shown by the dashed and dotted magenta lines from our higher resolution 2×256^3 particle simulations with σ-derived winds with AGB feedback. The metal enrichment of the IGM at early times is significantly higher when the SF from smaller galaxies is included; therefore, we use only higher resolution models to explore the IGM enrichment at $z > 2$. Also, our models suggest an overestimated SFRD at the lowest redshifts. This indicates that some other form of feedback is needed to suppress SF in massive galaxies at late times (such as AGN feedback; e.g. Cattaneo et al. 2007).

The three models shown, the Φ-derived winds and the σ-derived winds with and without AGB feedback, are indistinguishable in their global SFRDs above $z = 4$ because the mass loading factor and not wind speed is the largest determinant of SF (OD06). As explained in OD06, the earliest wind particles have not had time to be re-accreted by galaxies; therefore, the SFR is regulated purely by how much mass is ejected (η). The faster wind velocities of the Φ-derived model at $z < 2$ decrease SF relative to the σ-derived model, because wind particles are sent farther away from galaxies making this gas harder to re-accrete while also heating the IGM more and further curtailing SF. We will quantify this recycling of winds in Section 5.

The average virial ratio of winds ($E_{\rm rat}$), defined as the ratio of the kinetic energy to the potential at the launch position ($0.5\,v^2_{\rm wind}/(-\Phi)$), in the upper right-hand panel shows how σ-derived winds inject progressively less energy into their surroundings with time. $E_{\rm rat}$ should be invariant across time for Φ-derived winds in its simplest form, but falls sharply below $z = 1$ due to our wind speed limits, and rises slightly at high z due to the metal-dependent $v_{\rm wind}$. The faster Φ-derived winds spatially distribute more metals (solid lines in lower left-hand panel) and heat the IGM (lower right-hand panel) to a greater extent than the σ-derived winds. We will show in Section 4.2 that the cooler, less-enriched IGM of the σ-derived wind models makes a significant difference in metals seen in quasar absorption line spectra. The gaseous metallicity (dashed lines in lower left-hand panel) is slightly higher in the Φ-derived wind model despite fewer overall stars formed, because fewer metals end up in stars.

Finally, we consider the impact of AGB feedback. AGB stars do not add any appreciable energy feedback, as demonstrated by the invariance in the $E_{\rm rat}$ and volume-averaged temperature in the models with (magenta lines) and without (blue) AGB feedback. However, AGB stars provide feedback in the form of returning gas mass to the ISM, which is now available to create further generations of stars. For instance, with AGB feedback the SFRD at $z = 0$ is increased by nearly a factor of 2 compared to without. Hence, models that do not include such stellar evolutionary processes may not be correctly predicting the SFRD history.

Downloaded from https://academic.oup.com/mnras/article/387/2/577/1022513 by guest on 16 August 2022

4 THE UNIVERSAL METAL BUDGET

In this section, we will investigate what the sources of cosmic metals are, and where these metals end up. To do so, we examine quantities summed over our entire simulation volumes, with special attention to the three different sources of metals: Type II SNe, Type Ia SNe, and AGB stars. We also discuss the impact of AGB feedback and σ-derived winds.

4.1 Sources of metals

4.1.1 The stellar baryonic content

Since stars produce metals, we first examine the evolution of the stellar baryonic content. The key aspect for metal evolution is that stellar recycling provides new fuel for SF. For the Chabrier IMF assumed in our simulations, SNe return ∼20 per cent of stellar mass instantaneously back into the ISM (which is double that for a Salpeter IMF), and delayed feedback will eventually return another ∼30 per cent over a Hubble time-scale. With half the gas being returned to the ISM, most of it (∼80 per cent) on time-scales of less than a Gyr, subsequent generations of stars can form, leading to greater metal enrichment. The difference between σ-derived wind models with and without AGB feedback in the SFRD plot (upper left-hand panel of Fig. 4) demonstrates how AGB feedback makes available more gas for SF at later times.

Despite more SF in the l64n256vzw-σ model with AGB feedback, slightly more mass is in stars at $z = 0$ in the no-AGB feedback model by $z = 0$ '$\Omega_*(z = 0)/\Omega_b = 0.081$ versus 0.071' since there is no mass loss from long-lived stars. However, if we count all stars (including short-lived stars undergoing SNe) formed over the lifetimes of our simulated universes, the AGB feedback model forms 37 per cent more stars [$\Omega_*(\mathrm{all})/\Omega_b = 0.138$ versus 0.101]. This is the more relevant quantity when considering the metal budget of the local Universe. Another way to think of this is that the stars in today's local Universe account for [$\Omega_*(z = 0)/\Omega_*(\mathrm{all})$=] 52 per cent of all the stars that have ever existed, assuming that the mass in short-lived stars is negligible (a safe assumption in the low-activity local Universe).

Fig. 5 shows the amount of baryons formed into stars, $\delta\Omega_*$ (i.e. the SFR), and the amount of stellar mass lost via delayed feedback, $\delta\Omega_{\mathrm{del}}$, as a function of time. The ratio $\delta\Omega_{\mathrm{del}}/\delta\Omega_*$ increases as more generations of stars are continuously formed with each generation contributing to $\delta\Omega_{\mathrm{del}}$. The quantity $\delta\Omega_{\mathrm{del}}/\delta\Omega_*$ should approach 0.3 for a steady SFR in a Hubble time, because 30 per cent of the stellar mass is returned via delayed feedback, but this is actually exceeded since the SF is declining at late times. The amount of material lost via delayed feedback over the history of the Universe is found by subtracting the stars at $z = 0$ from the number of long-lived stars formed over the history of the Universe.

$$\Omega_{\mathrm{del}} = \int_{0\,\mathrm{Gyr}}^{14\,\mathrm{Gyr}} \delta\Omega_*(t)(1 - f_{\mathrm{SN}})\,\mathrm{d}t - \Omega_*(z = 0), \quad (8)$$

where we assume that $\Omega_*(z = 0)$, the stars in today's Universe, has a negligible quantity of short-lived stars. The amount of delayed feedback is $\Omega_{\mathrm{del}} = 0.039$ or 55 per cent of the stellar baryons in today's Universe, which is a significant quantity.

4.1.2 The metal content

We segue into our discussion of metals by plotting the global production of the four species tracked by their source (Type II SNe, Type Ia SNe, or AGB stars) in the left-hand panels of Fig. 6. Metals produced by Type II SNe depend on the current SFR ($\delta\Omega_*$), which is apparent by the fact that the solid lines in the left-hand panels have roughly the similar shape to the global stellar mass accumulation rate (Fig. 5). Type II SNe dominate the enrichment for all four elements at all redshifts; hence, global chemical enrichment is reasonably approximated by current SF alone.

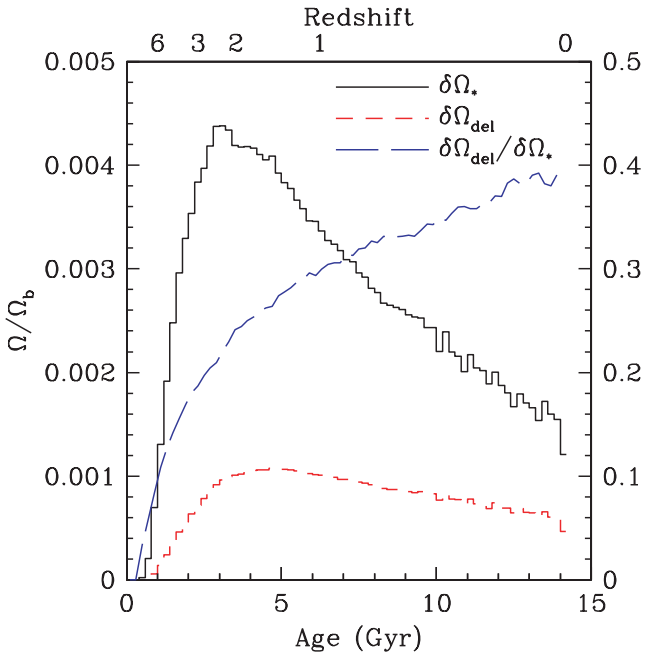

Figure 5. Global quantities binned in 200 Myr bin of stars formed ($\delta\Omega_*$, solid black line) and mass lost via delayed feedback ($\delta\Omega_{\mathrm{del}}$, dashed red line) relative to Ω_b in the $32\,h^{-1}$ Mpc 2×256^3 simulation. The ratio of the two is the long-dashed blue line.

Dividing the amount of each type of metal formed via Type II SNe by Ω_* gives the SN yield of that element shown as the solid lines in the right-hand panels of Fig. 6. These yields should and do match the Type II SNe yield tables that are an input to the simulations. The yields do not evolve significantly because there is only weak metallicity dependence in the Limongi & Chieffi (2005) yields employed here. Note that previous work has generally assumed no metallicity dependence. Above $z = 6$, the yields are slightly lower due to less metals injected by low-metallicity stars. A slight upturn is notable at lower redshift for carbon and silicon as their yields increase with metallicity.

Turning to metals injected via AGB feedback (dashed red lines in Fig. 6), we find more complex behaviour that varies among the species. The left-hand panels show that AGB feedback is an important source of carbon (∼30 per cent by $z = 0$), iron and silicon (both ∼25 per cent by $z = 0$), but is a negligible contributor for oxygen. Dividing these values by Ω_{del} results in the global AGB yields as a function of redshift in the right-hand panels. For carbon and oxygen, these are a summation of the yield values in our input tables for all stars of various ages and metallicities undergoing AGB feedback.

The carbon yields shows the most interesting evolution, which are indicative of the underlying processes of stellar evolution in different stars. As explained in Section 2.1.3 and shown in Fig. 1, the most-massive and short-lived AGB stars (4–8 $\mathrm{M}_\odot$) have hot-bottom burning that destroys carbon; these are the stars losing mass via AGB feedback the most at very high z. Between 2 and 4 $\mathrm{M}_\odot$,

Downloaded from https://academic.oup.com/mnras/article/387/2/577/1022513 by guest on 16 August 2022

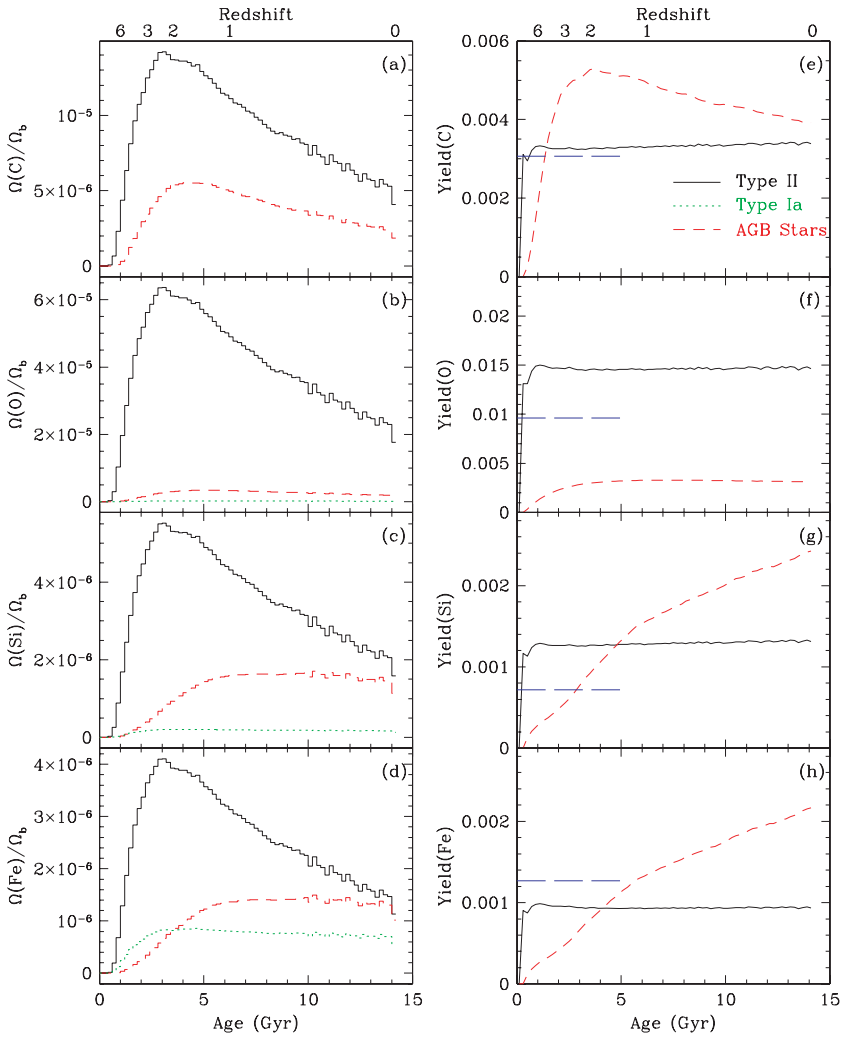

Figure 6. Metal production by species relative to Ω_b along with their yields plotted in 200 Myr bins in the $32\,h^{-1}$ Mpc 2×256^3 simulation. Panels (a), (b), (c) and (d) trace the amount of carbon, oxygen, silicon and iron, respectively, returned to the gas phase by Type II SNe (black solid lines), Type Ia SNe (green dotted lines), and AGB stars (red dashed lines). The yields for the various species are calculated in panels (e)–(h) by taking lines in panels (a)–(d) and dividing by the matching line types in Fig. 5; the long-dashed lines in the left-hand panels indicate Anders & Grevesse (1989) solar values. Type II SNe yields remain relatively constant despite metallicity-dependent yields. The AGB carbon yields strongly depend on z and peak when 2–4 $M_\odot$ die. AGB silicon and iron yields are simply reprocessed metals formed in SNe and reflect the ensemble metallicities of all stars undergoing AGB feedback at a given redshift.

the third dredge-up makes AGB stars into carbon stars with very high carbon yields from stars dying 200 Myr to 1 Gyr after their formation. At $z \sim 2$, carbon stars dominate the carbon yields, but then less-massive stars ($< 2\,M_\odot$) without the third dredge-up begin to reach the AGB phase, and the ensemble AGB carbon yield begins to decline.

Oxygen is burned in AGB stars, resulting in a net decrease in its overall content as a result of delayed feedback. Accounting for a minor contribution from Type Ia SNe, the vast majority of gaseous oxygen is synthesized in Type II SNe. Hence, oxygen is the ideal species to trace the cosmic evolution of Type II SNe.

The AGB yields of silicon and iron may at first be surprising considering that AGB stars do not process these elements. These yields reflect the ensemble metallicities of mass loss from AGB stars, since they neither create nor destroy heavier elements at any significant rate, but instead simply regurgitate them. Most surprising is that more iron is ejected from AGB stars than Type Ia SNe. The difference between these two forms of feedback associated with stars is that the iron yield of Type Ia SNe is nearly a half (i.e. $0.6\,M_\odot$ formed per $1.4\,M_\odot$ SNe) and should significantly enrich its local environment, while the iron lost from AGB stars should have a slightly lower yield than the surrounding gas metallicity since these stars are older and hence less enriched.

It is curious and probably not correct that iron and silicon AGB yields exceed solar metallicities by as much a factor of 2–3 by $z = 0$. This means that at $z = 0$, the average AGB star is at least (2–3) $Z_\odot$, which is almost definitely too high when stars younger than the Sun in the Milky Way disc are $\sim Z_\odot$ (Twarog 1980). Even though most $z = 0$ AGB mass loss comes from stars younger than the Sun since most AGB feedback occurs within 1 Gyr for a Chabrier IMF, the extremely supersolar metallicities are indicative of too much late SF. Reasons for this include too much SF in massive systems in our simulations, as well as our slightly high value of $\Omega_b = 0.048$ (instead of the currently more canonical $\Omega_b = 0.044$).

Table 2 summarizes the sources of metals at $z = 2$ (roughly 10^{10} yr ago) and $z = 0$ for the l32n256vzw-σ simulation. These

Downloaded from https://academic.oup.com/mnras/article/387/2/577/1022513 by guest on 16 August 2022

Table 2. Sources of feedback.

Species	Ω/Ω_b	Per cent Type II SNe	Per cent Type Ia SNe	Per cent AGB stars	Per cent AGB processing
$z = 2$					
Baryons	–	0.87	.0016	0.83	–
Carbon	1.677e−04	85.70	0.0[a]	23.25	+14.30
Oxygen	6.123e−04	105.4	0.32	3.48	−5.75
Silicon	5.642e−05	96.50	3.57	9.30	+0.00
Iron	5.013e−05	83.49	16.51	9.23	+0.00
$z = 0$					
Baryons	–	3.74	.0098	5.42	–
Carbon	6.566e−04	95.35	0.0[a]	38.29	+4.65
Oxygen	2.194e−03	126.1	0.52	7.68	−26.60
Silicon	2.549e−04	95.29	4.72	33.89	+0.00
Iron	2.265e−04	78.32	21.68	33.16	+0.00

[a]These models were run with no Type Ia yields for carbon. These carbon yields are fractionally insignificant anyway.

can be compared to available observational constraints. Using oxygen, the global metallicity averaged over all baryons is $\langle Z_b \rangle (z = 2) \sim 0.064\,Z_\odot$ rising to $\langle Z_b \rangle (z = 0) \sim 0.23\,Z_\odot$. These values are remarkably similar to those derived by Bouché et al. (2007) (hereafter B07) [$\langle Z_b \rangle (z = 2) \sim 0.056$ and $\langle Z_b \rangle (z = 0) \sim 0.20\,Z_\odot$] where they assumed a Salpeter IMF weighted metallicity yield of 0.024 and integrated over the SF history of the Universe from Cole et al. (2001). While encouraging, this comparison is highly preliminary owing to many systematics, such as the fact that our simulations produce too many stars overall, and the assumption of a Salpeter IMF at all times is probably not consistent with observations (see e.g. Davé 2008, and discussions therein). It is hoped that improving observations will enable more interesting constraints on cosmic chemical evolution models.

While it is well known that Type II SNe dominate carbon, oxygen, and silicon production, it may be somewhat surprising for iron, considering that Type Ia SNe are often assumed to be the primary producers of iron; however, this is actually only true in environments dominated by older stars. Long-lived stars also destroy oxygen, eliminating 20 per cent of the oxygen formed by Type II SNe. Processing of oxygen by AGB stars helps to move oxygen abundances from α-enhanced levels to solar levels. Of course, long-lived stars do make a net surplus of both carbon and oxygen in post-main-sequence nucleosynthesis; however, most of these metals remain locked in stellar remnants, which we do not track in our simulations and are not included in this table. Fukugita & Peebles (2004) estimate a $\langle Z_b \rangle (z = 0) \sim 0.68\,Z_\odot$ for all metals including those in remnants, which exceeds the metals not locked up (i.e. the ones we track) by a factor of a few.

Even though AGB feedback injects an appreciable amount of carbon into surrounding gas (∼40 per cent of carbon injected via Type II SNe), the net surplus of carbon resulting from AGB feedback is only ∼5 per cent of Type II SNe by $z = 0$, because much of this carbon is coming from stars with high metallicity already. Carbon stars (∼ 2–4 $M_\odot$) add to the overall cosmic carbon abundance while higher and lower mass AGB stars reduce the amount of carbon. A larger impact on carbon production comes from recycled gas that enables more Type II SNe; as noted before, 37 per cent more stars form in simulations that include AGB feedback. Stars also lose mass via AGB feedback when they have moved away from the sites of their formation, and can directly enrich metal-poorer areas such as the ICM and intragroup medium. Hence, the location of feedback from AGB stars and Type Ia SNe turns out to be important for understanding enrichment in various environments. We consider this topic next.

4.2 The location of metals

B07 calculated from observations that metals migrated from gas to stars between $z = 2 \rightarrow 0$ as metals fall back into the deeper potential wells of growing galaxies, and are more likely to remain there as SF-driven winds decline at low z. Our new simulations generally agree with the results of B07 that about one-third of metals are in stars at $z = 2$, increasing to two-thirds by $z = 0$.

In Fig. 7, we subdivide mass and metals further by their baryonic phases. The top panel shows the baryonic fraction in diffuse gas ($T < 10^5$), warm-hot intergalactic medium (WHIM) gas ($10^5 < T < 10^7$), hot gas in clusters ($T > 10^7$), and galaxies (stars and ISM) for the l64n256vzw-σ, l64n256vzw-σ-nagb, l32n128vzw-Φ models as a function of redshift. The steady transfer of gas from diffuse to WHIM and hot IGM between $z = 3 \rightarrow 0$ was first noted by Cen & Ostriker (1999) and Davé et al. (1999), and our current results are similar to those from Cen & Ostriker (2006) using nearly the same cosmology. The addition of AGB feedback does not appreciably change any of these values.

σ-derived winds have 5 per cent fewer baryons in the WHIM than Φ-derived winds at $z = 0$ due to weaker winds at late times. Cen & Ostriker (2006) find that their baryon fraction in the WHIM increases by about 10 per cent owing to galactic superwinds, which matches our results (not shown). The metal fraction in the WHIM is basically constant in the σ-derived winds, in stark contrast to the Φ-derived wind model (green lines; also see Fig. 1 of DO07), which shows that fraction of metals in WHIM grow steadily from $z = 4 \rightarrow 0$, reaching 25 per cent today. The much slower σ-derived wind velocities at late epochs are mostly unable to shock-heat metals above temperatures where metal-line cooling dominates, and instead the gas cools efficiently. Although the addition of AGN feedback is unlikely to change the metal content of baryons by more than a few per cent (B07), the effect of $>1000\,km\,s^{-1}$ winds from quasi-stellar objects such as those observed by Tremonti, Moustakas & Diamond-Stanic (2007) could be appreciable for metals in the WHIM and hot phases.

The total metal budget by baryonic phase in the second panel shows a minor change owing to AGB feedback, namely that 5 per cent less metals are found in the galaxies, with those metals instead being located in the diffuse IGM. This is because increased

Downloaded from https://academic.oup.com/mnras/article/387/2/577/1022513 by guest on 16 August 2022

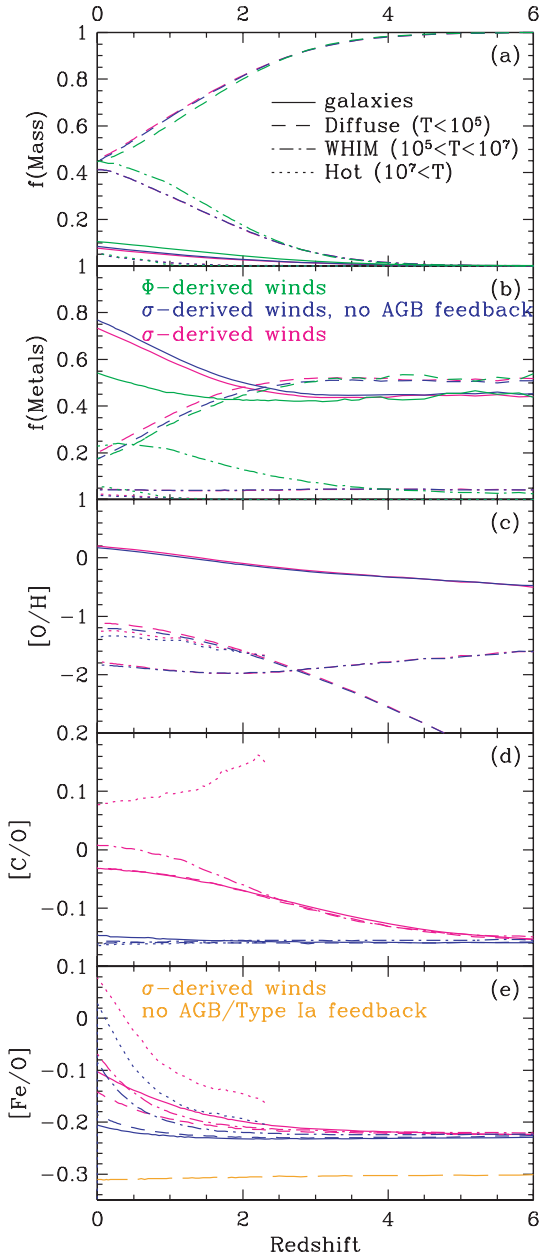

Figure 7. The evolution of of mass and metals by baryonic phase in the $64\,h^{-1}$ Mpc, 2×256^3 simulations with and without AGB feedback, and the $32\,h^{-1}$ Mpc, 2×128^3 simulation with the old potential-derived winds (shown only in top two panels). The slower σ-derived winds at low redshift do not inject nearly as many metals into the WHIM. The addition of AGB feedback does not change the baryonic mass fractions (panel a) and increases slightly the amount of metals in galaxies (panel b). Oxygen metallicity (panel c), which traces Type II SNe, remains nearly unchanged, but delayed feedback boosts carbon relative to oxygen (panel d), and iron increases at late times relative to oxygen (panel e) in hot gas mostly due to Type Ia SNe. The global [Fe/O] in a test simulation without any delayed feedback is shown as the long-dashed orange line in panel (e).

SF from gas made available via delayed feedback results in more winds that expel metals.

4.2.1 Oxygen in the WHIM

The third panel of Fig. 7 shows the oxygen metallicity in various baryonic phases. Overall, oxygen metallicities ([O/H]) remain nearly identical (within 0.1 dex) with the addition of AGB feedback. The 37 per cent increase in SF and therefore oxygen production from Type II SNe is counterbalanced by a 20 per cent decrease due to the AGB processing of oxygen. Galactic baryons show slightly supersolar oxygen abundance, while the abundances in diffuse and hot phases are nearly one-tenth solar.

The WHIM oxygen abundance is relatively constant with redshift, and shows [O/H] $= -1.76$ at $z = 0$. Our simulations produce two distinct types of WHIM: (1) the unenriched majority formed via the shock heating resulting from structural growth, and (2) the WHIM formed by feedback, which is significantly enriched. The weaker σ-derived winds form very little of the latter. While simulations suggest, by comparison with observed O VI absorbers, that the WHIM metallicity should be around one-tenth solar (Cen et al. 2001; Chen et al. 2003), it remains to be seen whether the σ-derived winds are in conflict with O VI observations. Since O VI arises in both photoionized and collisionally ionized gas, it could be that enough O VI is present in photoionized gas to explain the observed number density of such systems. Moreover, non-equilibrium ionization effects could be important (Cen & Fang 2006). A careful comparison with O VI observations is planned, but is beyond the scope of this paper.

For now, we note that the oxygen abundance in the WHIM may be an interesting probe of feedback strength. Sommer-Larson & Fynbo (2008) come to the same conclusion at $z = 3$ when tracing oxygen content by temperature, noting that the stronger feedback by a top-heavy IMF produces significantly greater amounts of oxygen in the WHIM. Extremely fast winds ($v_{\rm wind} > 1000\,{\rm km\,s^{-1}}$) emanating from AGN (Tremonti et al. 2007) will also create more enriched WHIM.

4.2.2 Carbon in the IGM

In the bottom two panels of Fig. 7, we show the carbon and iron abundance relative to oxygen, a tracer of Type II SN enrichment, to emphasize the differences in these two species influenced by delayed feedback. For carbon especially, AGB feedback has a significant impact. [C/O] evolution shows an obvious increase even at high z, because the time-scale for mass loss from carbon stars is 0.2–1 Gyr. Every phase appears to evolve similarly with their lines sometimes blending in Fig. 7 except the hot phase, which has at least 50 per cent more carbon at $z > 2$. Carbon stars lose their mass near sites of SF, and this carbon is then blown out and shock-heated by a second generation of SNe. The net effect of AGB feedback on the $z = 0$ carbon metallicity is $+0.22$, $+0.25$ and $+0.33$ dex for diffuse, WHIM and hot IGM, respectively. This results in abundance ratios close to solar in all phases.

A basic observational test of IGM enrichment models is the evolution of Ω(C IV), that is, the mass density in C IV systems seen in quasar absorption lines. In Fig. 8, we plot Ω(C IV) from $z = 6 \rightarrow 0$ (see OD06 for exact method of computing Ω(C IV)) to see the effect of σ-derived winds and AGB feedback. In OD06 we reproduced the relative invariance in the observed trend of Ω(C IV) between $z = 5 \rightarrow 2$ by counterbalancing the increasing IGM carbon content by a similarly lowering C IV ionization factor; the new σ-derived models also match the observed trend quite well, for a similar reason. The addition of AGB feedback increases Ω(C IV) by 70 per cent ($+0.23$ dex) at $z \lesssim 0.5$, leading to a value consistent within the error bars of $z \approx 0$ measurement by Frye et al. (2003).

The main reason is that AGB feedback adds new fuel for SF, resulting in more C IV expelled into the IGM at late times. Compared to the Φ-derived winds, the σ-derived winds push out more metals

Downloaded from https://academic.oup.com/mnras/article/387/2/577/1022513 by guest on 16 August 2022

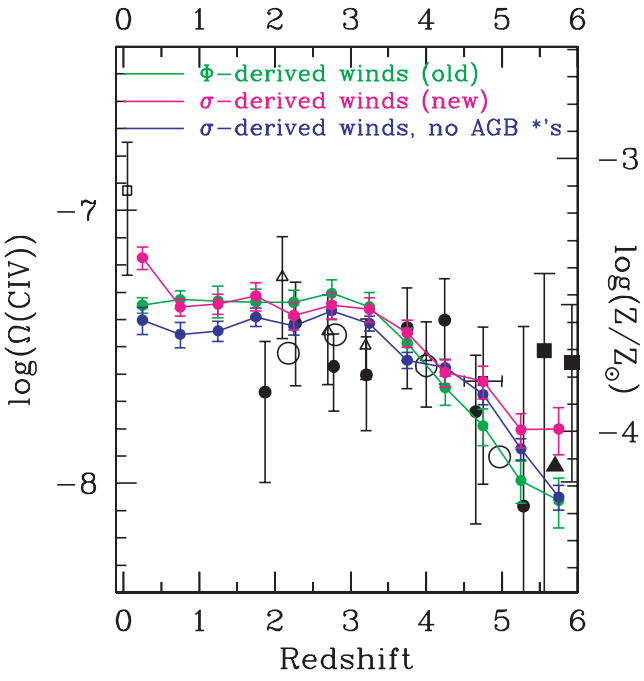

Figure 8. Evolution of Ω(C IV) from $z = 6 \rightarrow 0$ for the Φ-derived wind model with AGB feedback (green) and the σ-derived wind model with and without AGB feedback (magenta and blue). Our models are compared to observations from Songaila (2001) (black circles), Pettini et al. (2003) (small filled black squares), Bokensberg, Sargent & Rauch (2003) (open triangles), Frye et al. (2003) (open square), Songaila (2005) (large open dots), Simcoe (2006) (large black squares), and Ryan-Weber et al. (2006) (black triangle is a lower limit). While all models appear to fit the majority of the data, there are subtle differences that we highlight between our models. The new σ-derived winds distribute metals more broadly boosting Ω(C IV) at $z > 5$, while more carbon resulting from AGB feedback enriches the IGM in the local Universe. The three data points below $z = 1.5$ are calculated from $8\,h^{-1}$ Mpc 2×128^3 simulations and from $16\,h^{-1}$ Mpc 2×256^3 elsewhere, except in the case of the σ-derived winds without AGB feedback in which case only the small box is used.

early better matching the high-z C IV observations of Ryan-Weber, Pettini & Madau (2006) and Simcoe (2006). The faster Φ-derived winds at low z raise the temperature of the metal-enriched IGM while pushing the metals to lower overdensities and lowering the C IV ionization fraction.

The σ-derived wind model with AGB feedback is the first model we have explored that is able to fit the entire range of Ω(C IV) observations from $z \sim 6 \rightarrow 0$.

The σ-derived wind model with AGB feedback achieves higher Ω(C IV) at $z > 5$ and $z < 1$ that at face value improves agreement with observations. While these data are uncertain and hence one should not overinterpret this improved agreement, the main point of this exercise is to show how our newly incorporated physical processes could have observational consequences. Furthermore, the results are to be taken with caution, owing to the small box size of our simulations ($8\,h^{-1}$ Mpc 2×128^3) below $z = 1.5$; this volume is not nearly large enough to form the large-scale structures in the local Universe. It is encouraging that the values derived from this small box agree within the error bars with the larger l16n256vzw-σ simulations above $z = 1.5$. Future observations at low z by the Cosmic Origins Spectrograph, and at high z with advances in near-infrared spectroscopy will allow more relevant and detailed comparisons.

4.2.3 *Iron in the ICM*

The [Fe/O] evolution (bottom panel of Fig. 7) is dominated by Type II SNe until $z \sim 2$, at which point delayed feedback processes of Type Ia SNe and AGB stars become important. The instantaneous component of the Type Ia SNe adds 19 per cent of the Type II SN iron yield, which raises the [Fe/O] everywhere from -0.30 to -0.23 (compare to global [Fe/O] in a simulation without any Type I SNe or AGB feedback[2]). The delayed component of Type Ia SNe adds only 9 per cent more of the Type II SNe iron content generated over the lifetime of the Universe. However, the combination of the high iron yield (0.43) and the location of enrichment often being low-metallicity regions away from the sites of SF means delayed Type Ia SNe can have a significant observational signature in a low-density medium such as the ICM. The net increase of all Type Ia SNe (delayed and instantaneous) on the $z = 0$ iron content is $+0.32$ dex in the hot component and $+0.21$ dex in the WHIM. AGB feedback increases iron content by allowing 37 per cent more stars to form; this extra iron primarily remains in galaxies, but increases iron in the hot component by $+0.15$ dex and the WHIM by $+0.07$ dex. Overall, the hot iron metallicity increases by nearly three times with the addition of Type Ia and AGB feedback.

To demonstrate the effect on observables, we calculate the free–free emission-weighted [Fe/H] of the ICM in clusters/groups with temperatures in excess of 0.316 keV at $z = 0$ in the l64n256vzw models to simulate the X-ray observations. We identify large bound systems in the simulations using a spherical overdensity algorithm (see Finlator et al. 2006, for description). The average of over 130 clusters/groups is -1.11 without any delayed feedback, -0.78 with Type Ia SNe included, and -0.57 with AGB feedback also included. Hence, the addition of delayed forms of feedback increases the ICM [Fe/H] by 3.4 times. This is now in the range for the canonical ICM metallicities of around 0.3 solar, as well as for groups between 0.316 and 3.16 keV as observed by Helsdon & Ponman (2000) (they found $-0.60 <$ [Fe/H] < -0.36). Of course, X-ray emission at $\sim$1 keV has a significant contribution from metal lines, and observations can be subject to surface brightness effects (e.g. Mulchaey 2000), so this comparison is only preliminary. A more thorough comparison of simulations to ICM X-ray observations is in preparation (Davé, Sivanandam & Oppenheimer, in preparation).

To summarize this section, we showed that Type II SNe remain the dominant mode of global production for each species we track, usually by a large margin. When considering metals not locked up in stellar remnants (i.e. observable metals), Type Ia SNe only produce 22 per cent of the cosmic iron and AGB stars only contribute 5 per cent to the cosmic carbon abundance. Mass feedback from long-lived stars allows metals to be recycled and form new generations of stars, increasing late-time SF by $\sim$30–40 per cent. More importantly, the location of metals injected by delayed modes of feedback can significantly impact metallicities in specific environments. The IGM carbon content, probably the best current tracer of IGM metallicity, increases by 70 per cent by $z = 0$ when AGB feedback is included. The iron content observed in the ICM at least triples, primarily due to Type Ia SNe. Delayed metallicity enrichment appears to heavily affect the enrichment patterns of the low density gas of the IGM and ICM where there are relative few metals, compared to galaxies where we find the metallicity signatures of Type II SNe dominate. Although our simulations do not produce large passive

[2] We ran a l32n128vzw-σ test simulation with only Type II feedback, and the only major difference is the lack of iron produced via Type Ia SNe relative to l32n128vzw-σ-noagb.

Downloaded from https://academic.oup.com/mnras/article/387/2/577/1022513 by guest on 16 August 2022

systems at the present epoch, it is likely that delayed modes of feedback will be important for setting the metallicity in and around such systems as well. Hence, incorporating delayed feedback is necessary to properly understand how metals trace SF in many well-studied environments.

5 GALAXIES AND FEEDBACK

Thus far, we have examined energy balance and metallicity budget from a global perspective. In this section, we investigate such issues from the perspective of individual galaxies. We will answer such questions as: what galaxies are dominating each type of feedback (mass, energy, and metallicity)? How does this evolves with redshift? Do winds actually leave galaxy haloes and reach the IGM? What types of galaxies are enriching the IGM at various epochs? The key concept from this section is wind recycling; that is, the products of feedback do not remain in the IGM, but instead are either constantly cycled between the IGM and galaxies or never escape their parent haloes in the first place, and are better described as halo fountains.

During each simulation, all particles entering a wind are output to a file. The originating galaxy is identified, and the eventual reaccretion into star-forming gas is tracked. In this way, wind recycling can be quantified in galaxy mass and environment. Throughout this section, we will use SKID-derived galaxy masses, which match our on-the-fly FOF galaxy finder for the vast majority of cases (cf. Section 2.2). We use our favoured σ-derived wind simulations in our following analysis, unless otherwise mentioned.

5.1 Feedback as a function of galaxy mass

Fig. 9 quantifies mass (upper left), metal (upper right) and energy (lower panels) feedback, as a function of galaxy mass in our σ-derived wind simulations at four chosen redshifts ($z = 6$, 4, 2, 0.5). We choose $z = 0.5$ to represent the local Universe rather than $z = 0$, because we want to follow the evolution of wind materials after they are launched and consider 5 Gyr a compromise as enough time for the winds cycle to play out, but not too much such that the cosmological evolution is overly significant. The upper left-hand panel shows the mass-loss rate in outflows as a function of galaxy baryonic mass. At a given galaxy mass, the outflow rate goes down with time, by roughly a factor of 10 from $z = 6 \rightarrow 0.5$. Remember that this is the rate of mass being driven from the galaxy's star-forming region; whether the material makes it to the IGM or remains trapped within the galactic halo will be examined later.

Along with the results of our simulations, we plot two simple 'toy models' of feedback behaviour corresponding to galaxies forming stars at constant specific SFRs (i.e. SFR per unit stellar mass) of 1.0 and 0.1 Gyr^{-1}; these roughly correspond to typical star-forming galaxies at $z = 6$ and 0.5, respectively. The momentum-driven wind

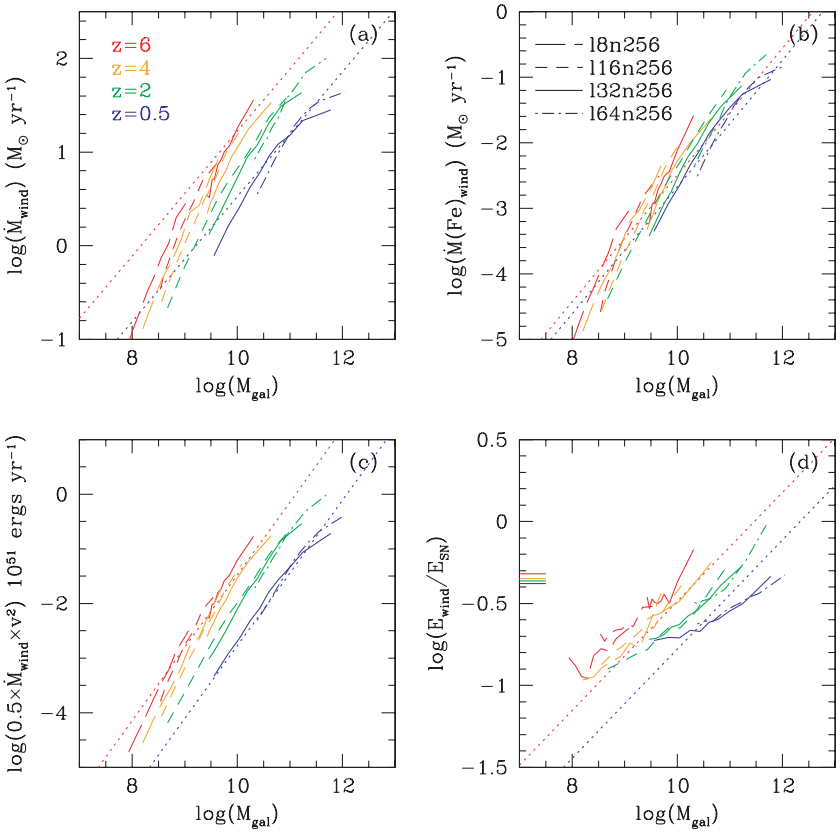

Figure 9. Feedback properties are shown as a function of galaxy mass (derived by SKID) for four redshifts for our σ-derived wind simulations at various box sizes. The red and blue dotted lines are our 'toy models' calculated using momentum-driven wind relations and assuming specific SFRs of 0.1 and 1.0 Gyr^{-1}, and metallicities of $Z = 0.3\,\mathrm{Z}_{\odot}$ and 1.0 for $z = 6$ and 0.5, respectively. Mass and metal feedback (panels a and b) are predicted to go as $M_{\mathrm{gal}}^{2/3}$, although metallicity feedback additionally depends on the gas mass–metallicity of galaxies, where $Z \propto M_{\mathrm{gal}}^{0.3}$. Energy feedback, in 10^{51} erg units (panel c) follows the predicted $M_{\mathrm{gal}}^{4/3}$ relation very closely, and the ratio wind energy efficiency, $E_{\mathrm{wind}}/E_{\mathrm{SN}}$, (panel d) rises nearly as $M_{\mathrm{gal}}^{1/3}$ for most redshifts. The lines on the left-hand side of panel (d) show the average $E_{\mathrm{wind}}/E_{\mathrm{SN}}$ efficiency in the l32n256 box is declining slightly, although these values may be lower when lower mass galaxies not resolved in this box are included.

© 2008 The Authors. Journal compilation © 2008 RAS, MNRAS **387,** 577–600

Downloaded from https://academic.oup.com/mnras/article/387/2/577/1022513 by guest on 16 August 2022

model predicts that mass feedback should go as $\dot{M}_{\rm wind} \propto {\rm SFR}/\sigma \propto {\rm SFR} \times M_{\rm gal}^{-1/3}\, H(z)^{-1/3}$. Making the reasonable assumption that ${\rm SFR} \propto M_{\rm gal}$ as typically found in simulations (e.g. Davé 2008), then this simple model would predict $\dot{M}_{\rm wind} \propto M_{\rm gal}^{2/3} H(z)^{-1/3}$. The dotted lines in Fig. 9 show these relations for our toy models. The red dotted line fits well to $z = 6$ at $M_{\rm gal} = 10^{9.5-10}\,{\rm M}_\odot$ showing these galaxies efficiently doubling their mass every 1.0 Gyr, while the doubling time is around 10 Gyr for galaxies at $z = 0.5$.

The typical mass outflow rate reduces with time for two reasons: first, the SFRs are lower owing to lower accretion rates from the IGM, as discussed in SH03b and OD06 and as observed by Pérez-González et al. (2005), Caputi et al. (2006) and Papovich et al. (2006). Secondly, galaxies grow larger with time and the mass loading factors drop, this even despite the $H(z)^{-1/3}$ factor that actually increases η for a galaxy of the same mass at lower redshift. Hence, the outflow rates qualitatively follow the trend seen in observations that at high redshifts outflows are ubiquitous and strong, while at the present epoch it is rare to find galaxies that are expelling significant amounts of mass.

Fig. 9, upper right-hand panel, shows the mass of metals launched as wind particles, which is $\dot{M}(Z)_{\rm wind} \propto M_{\rm gal}^{2/3} H(z)^{-1/3} Z_{\rm gal}$. For concreteness, we follow the iron mass, although other species show similar trends; recall that even at $z = 0$ 93 per cent of iron is produced in Type II SNe, and the fraction is higher at higher redshifts. This relation can be thought of as the $M_{\rm gal}$–$\dot{M}_{\rm wind}$ relation shown in the upper left-hand panel convolved with the SF-weighted gas mass–metallicity relations of galaxies at the chosen redshifts, since it is this gas that is being driven out in outflows. Finlator & Davé (2008) showed how our 'vzw' model reproduces the slope and scatter of the mass–metallicity relationship of galaxies as observed by Erb et al. (2006) for $z = 2$ LBGs. Again, we plot two dotted lines corresponding to our toy models with a $Z \propto M_{\rm gal}^{0.3}$ dependence accounting for the mass–metallicity relationship normalized to $z = 0.3$ and $1.0\,{\rm Z}_\odot$ at $10^{11}\,{\rm M}_\odot$ for $z = 6.0$ and 0.5, respectively. The two toy models show little evolution (0.18 dex decline from $z = 6 \rightarrow 0.5$, because the declining $\dot{M}_{\rm wind}$ is counterbalanced by an increasing metallicity for a given mass galaxy towards lower redshift. In the l32n256vzw-σ simulation, a $10^{10}\,{\rm M}_\odot\,{\rm yr}^{-1}$ galaxy injects $7.7 \times 10^{-3}\,{\rm M}_\odot\,{\rm yr}^{-1}$ of iron at $z = 6$ and $2.2 \times 10^{-3}\,{\rm M}_\odot\,{\rm yr}^{-1}$ at $z = 0.5$.

In the lower left-hand panel, we plot the total feedback energy per time (i.e. feedback power) imparted into wind particles as a function of galaxy mass. This power is $\dot{E}_{\rm wind} = 0.5\dot{M}_{\rm wind} \times v_{\rm wind}^2 \propto {\rm SFR} \times \sigma H(z)^{1/3} \propto M_{\rm gal}^{4/3} H(z)^{1/3}$, using the same assumption of ${\rm SFR} \propto M_{\rm gal}$. The feedback power is shown in units of 10^{51} erg yr^{-1}, which can be thought of as the number of SNe per year. Our simulations follow the trend of the toy models in terms of redshift evolution, and show an even tighter agreement at the low-mass end versus $M_{\rm gal}$ than the mass feedback; the metallicity dependence gives greater energies to winds from lower mass, less metal-rich galaxies. Energy feedback is an even stronger function of galaxy mass than mass or metallicity feedback.

The bottom right-hand panel in Fig. 9 shows feedback energy relative to SN energy from a Chabrier IMF ($E_{\rm wind}/E_{\rm SN}$). This quantity decreases with time, and increases with galaxy mass. The toy models shown represent $E_{\rm SN} \propto {\rm SFR} \propto M_{\rm gal}$ or $E_{\rm wind}/E_{\rm SN} \propto M_{\rm gal}^{1/3} H(z)^{1/3}$. At the low-mass end, the simulations rise above the toy model and show more scatter due to uncertainties in the the SFRs of the smallest galaxies, but the slope at most redshifts is correct. At the high-mass end, momentum-driven wind energy exceeds the SN energy, which is physically allowed since the UV photons produced during the entire lifetimes of massive stars drive winds in this scenario (see OD06, Fig. 4). Summing this ratio globally over all galaxies at each redshift, we obtain the values shown by the tick marks on the left-hand side of the panel. Globally, the average $E_{\rm wind}/E_{\rm SN}$ ratio is nearly one half at all redshifts, and is surprisingly constant, declining less than 0.1 dex from $z = 6 \rightarrow 0.5$ in the new σ-derived formulation of the winds. The decline of wind energy feedback for a given mass galaxy towards lower redshift is mostly counterbalanced by more massive galaxies driving more energetic winds at these redshifts. Less massive galaxies unresolved in the l32n256 box are likely to lower this value somewhat, so we only want to conclude that the wind energy is a significant fraction of SN energy and stays remarkably unchanged with redshift in the σ-derived momentum driven wind model.

To summarize, the momentum-driven wind simulations follow trends expected from the input momentum-driven outflow scalings. This is of course not surprising, and at one level this is merely a consistency check that the new wind prescription and the group finder are working correctly. However, this also gives some intuition regarding outflow properties as a function of galaxy mass required to achieve the successes enjoyed by the momentum-driven wind scenario. For example, mass outflow rates should correlate with galaxy mass, and outflow energy in typical galaxies is comparable to, and perhaps exceeds, the total available SN energy. These trends provide constraints on wind driving mechanisms and inputs to heuristic galaxy formation models such as semi-analytic models.

5.2 Feedback by volume

We shift from examining feedback trends in individual galaxies to studying feedback trends per unit volume. In order to facilitate observational comparisons, we use use stellar mass, M_*, rather than baryonic mass.

In Fig. 10, we plot histograms binned in 0.1 dex intervals of the three forms of feedback at five redshift bins from $z = 6 \rightarrow 0$ parametrized by the amount of feedback per cubic Mpc. These histograms include all SKID-identified galaxies in the 8, 16, 32, and $64\,h^{-1}$ Mpc boxes in order to obtain the large dynamical range covering over five decades of galaxy masses. The less computationally expensive l8n128vzw simulation was included in the histograms between $z = 0$ and 1.5 to probe the least-massive galaxies in this range, since the l16n256vzw run at the same resolution ends at $z = 1.5$. We also plot the median M_* of a galaxy contributing to each type of feedback shown as the vertical lines at the bottom of each panel.

The mass, energy, and metal outflow rates peak at increasingly higher galaxy masses with time. The galaxy mass resolution limits are $1.9 \times 10^7\,{\rm M}_\odot$ at $z \geqslant 4$ and $1.5 \times 10^8\,{\rm M}_\odot$ below; the peaks are mostly comfortably above these resolution limits, indicating that we have the necessary resolution to resolve the source of feedback across our simulation boxes for the three forms of feedback. The exceptions are the mass outflow rates at $z > 2$, which peak less than 1 dex from these limits. The changing resolution limit at $z = 4$ raises concern whether the evolution above and below this limit is real; however, the larger amount of evolution between $z = 4 \rightarrow 1$, despite an unchanging resolution limit shows that evolution at $z < 4$ is not just a resolution effect.

The median galaxy M_* expelling gas increases by $\sim$100 times between $z = 6 \rightarrow 0$, for all three forms of feedback. The vast majority of this growth occurs between $z = 6 \rightarrow 2$, where the median stellar mass increases by $\sim$30 times in just 2.3 Gyr. This is the epoch of peak SF in the Universe, so it is not surprising that galaxies show the most growth in their stellar masses then. The baryonic mass (stars plus gas, not shown) also jumps significantly, $\sim$10–15 times,

Downloaded from https://academic.oup.com/mnras/article/387/2/577/1022513 by guest on 16 August 2022

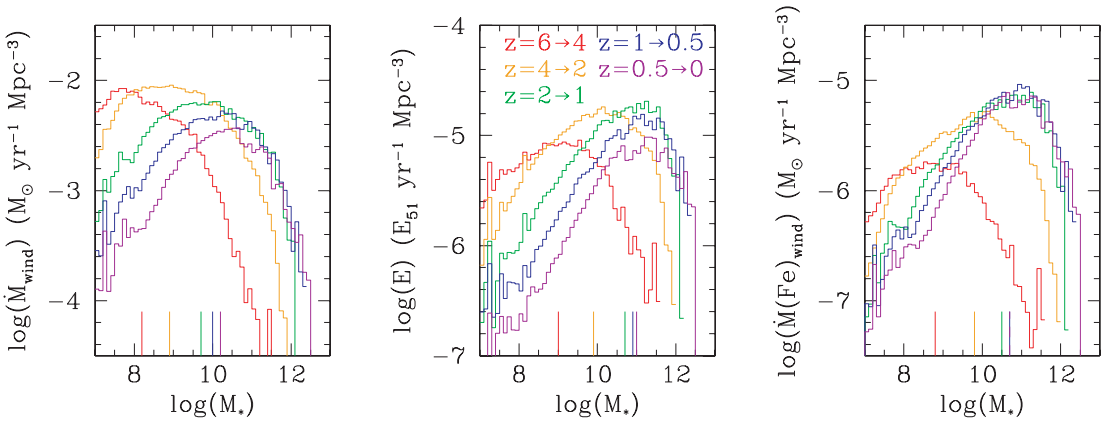

Figure 10. Mass, metallicity, and energy feedback per cubic Mpc binned by stellar mass (0.1 dex bins, derived by SKID) in five redshift bins covering $z = 6 \rightarrow 0$. The histograms include data from 8, 16, 32 and 64 h^{-1} Mpc in order to resolve a large range (five decades) of galaxy masses. The vertical lines with colours corresponding to their redshift range show the median galaxy producing each type of feedback. For all forms of feedback, the median M_* increases by a factor of 100 between $z = 6 \rightarrow 0$; most of this increase (30 times) is between $z = 6 \rightarrow 2$. However, each form of feedback favours a different mass-scale: $10^{10.2}$ $M_\odot$ for mass, $10^{11.0}$ $M_\odot$ for energy, and $10^{10.7}$ $M_\odot$ for metallicity. The mass resolution limits are 1.9×10^7 $M_\odot$ above $z = 4$ and 1.5×10^8 $M_\odot$ below.

but early small galaxies are more gas rich making the jump less extreme. Nevertheless, the evolution is much slower in the 10 Gyr between $z = 2 \rightarrow 0$ as both median M_* and $M_{\rm gal}$ at most triple and usually double in this longer time-span. This late growth could be an overestimate because of our overestimated SFRs at late times in the most-massive galaxies. It is quite possible that if our simulations could properly curtail massive galaxies from forming stars, median M_* would fall towards $z = 0$.

The same growth patterns for SF-driven feedback are also seen in the median galaxy weighted by SFR, which itself is highly correlated with $M_{\rm gal}$ as Davé (2008) shows using these same simulations. Therefore, the changing mass scales of SF-driven feedback reflect the hierarchical growth of galaxies between $z = 6 \rightarrow 0$, with most growth occurring before $z = 2$.

While it is no coincidence that all three forms of feedback show similar growth rates in median M_* (and $M_{\rm gal}$), each feedback form has a different mass preference and peaks at a different epoch. Mass feedback preferentially traces smaller galaxies due to the inverse relationship of η with $M_{\rm gal}$. High mass loading factors from small galaxies, which dominate SF at high redshift, are necessary to curtail the SF density at early times (OD06) and fit galaxy luminosity functions at $z > 3$ (Finlator et al. 2006; Bouwens et al. 2007). The mass feedback density peaks at $z \sim 3.5$ at 0.28 $M_\odot$ yr^{-1} Mpc^{-3}. The median galaxy in the relatively nearby Universe bin ($z = 0.5 \rightarrow 0$) has $M_* = 10^{10.2}$ $M_\odot$, or one-sixth the Bell et al. (2003) M^* value of $10^{11.0}$ $M_\odot$ in stellar mass.

The bottom right panel in Fig. 9 shows feedback energy relative to supernova energy from a Chabrier IMF ($E_{\rm wind}/E_{\rm SN}$). This quantity decreases with time, and increases with galaxy mass. The toy models shown represent $E_{\rm SN} \propto {\rm SFR} \propto M_{\rm gal}$, or $E_{\rm wind}/E_{\rm SN} \propto M_{\rm gal}^{1/3}(z)^{1/3}$. At the low-mass end, the stimulations rise above the toy model and show more scatter due to uncertainties in the star formation rates of the smallest galaxies, but the slope at most redshifts is correct. At the high-mass end, momentum-driven wind energy exceeds the supernova energy, which is physically allowed since the UV photons produced during the entire lifetimes of massive stars drive winds in this scenario (see OD06, fig. 4). Summing this ratio globally over all galaxies at each redshift, we obtain the values shown by the tick marks on the left-hand side of the panel. Globally, the average $E_{\rm wind}/E_{\rm SN}$ ratio is nearly one half at all redshifts, and is surprisingly constant, declining less than 0.1 dex from $z = 6 \rightarrow 0.5$ in the new σ-derived formulation of the winds. The decline of wind energy feedback for a given mass galaxy toward lower redshift is mostly counterbalanced by more massive galaxies driving more energetic winds at these redshifts. Less massive galaxies unresolved in the 132n256 box are likely to lower this value somewhat, so we only want to conclude that the wind energy is similar, is a significant fraction of SN energy and stays remarkably unchanged with redshift in the σ-derived momentum-driven wind model.

The metallicity feedback grows the fastest of all forms of feedback during the epoch of peak SF, and does not obtain its maximum density until slightly past $z = 1$ [$\dot{M}({\rm Fe})_{\rm wind} = 1.7 \times 10^{-4}$ $M_\odot$ yr^{-1} Mpc^{-3}]. The metallicity feedback is simply the mass feedback modified by the mass–metallicity relationship of galaxies, which favours higher M_* and lower redshift. The median M_* at $z = 0$ is 0.5 M^*, or approximately five times higher than the 0.1L^* median galaxy as determined by B07. However, we do not think that this is an inconsistency due to an overestimate in massive galaxy SF at low redshift, but instead a result of measuring different quantities. We are measuring the amount of feedback leaving a galaxy's star-forming region whereas B07 measures the feedback expelled from the galaxy reaching the IGM by determining the effective yield as a function of $v_{\rm rot}$. As we will show next, much of the mass and metals that are expelled never leave their parent haloes and are reaccreted in a time-scale often much less than the Hubble time. The leads us to introduce the important concept of wind recycling.

5.3 Wind recycling

What happens to the mass and metals once they are expelled from the galaxies' star-forming regions? Is all feedback best described as galactic superwinds or does some feedback never really escape from its parent halo and should more accurately be considered a halo fountain? To answer such questions, we introduce the concept of wind recycling, which plays an important role in feedback over cosmic time.

By following wind particles by their particle IDs during the simulation run, we can track how many times the same SPH particle is recycled in a wind. For the l32n256vzw-σ simulation evolved all the way to $z = 0$ we find that a wind particle is launched an average of 2.5 times; while 18.3 per cent of SPH particles are ever launched in a wind, the summed number of wind launches equals

Downloaded from https://academic.oup.com/mnras/article/387/2/577/1022513 by guest on 16 August 2022

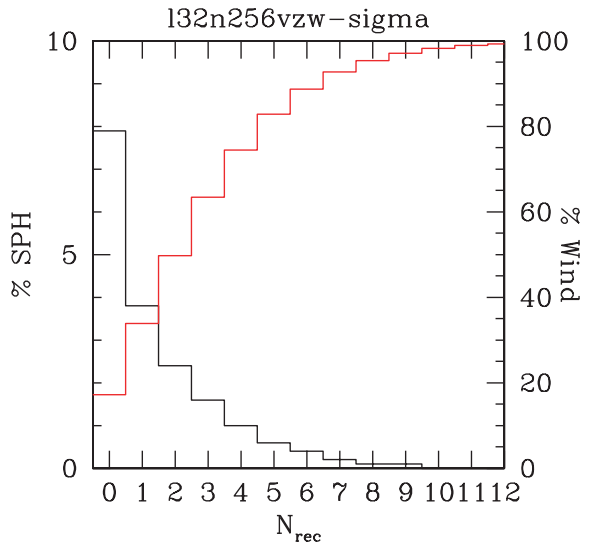

Figure 11. The percentage of all SPH particles recycled $N_{\rm rec}$ times by $z = 0$ in the $32h^{-1}$ Mpc 2×256^3 simulation is shown by the black histogram (left-hand scale). $N_{\rm rec} = 0$ means a wind particle is launched only once. The red line shows the cumulative sum of wind particles launched per bin (right-hand scale, normalized to 100 per cent) and is the sum of $(N_{\rm rec} + 1)$ multiplied by the black histogram added from the left-hand to the right-hand side. 50 per cent of winds are particles that have been or will be recycled three or more times indicating that wind recycling plays a significant if not dominant role in feedback.

45.7 per cent of the total number of SPH particles. Wind recycling dominates over winds being launched from galaxies for the first time– the average wind particle across time is more likely to have already been launched in a wind! The most important aspect is that wind material, once launched, cannot be assumed to be lost from the galaxy forever and remaining in the IGM. This is true despite the fact that, in our momentum-driven wind prescription, outflows are always ejected at speeds exceeding the escape velocity of its parent galaxy. Gravitational infall and hydrodynamic effects both conspire to slow down outflows and facilitate wind recycling.

Fig. 11 displays histograms of the number of times the same wind particle is recycled, $N_{\rm rec}$, in the l32n256 simulation. Only 17 per cent of all winds are particles ejected one time and therefore never recycled (i.e. $N_{\rm rec} = 0$); this corresponds to 7.9 per cent of all SPH particles. The record-holder is a particle recycled an astonishing 30 times indicating that probably in this case the term halo fountain may be more appropriate than galactic superwind. Perhaps the most-telling statistic is that half of the wind particles have been recycled three or more times. The continuous range in the number of recycling times blurs the distinction between a galactic superwind and a halo fountain, and suggests instead that there is a continuum.

The concept of recycling is not unexpected, and has been predicted by Bertone et al. (2007) from semi-analytical models. DO07 showed that metals move from mean cosmic density at $z = 2$ to an overdensity of 100 by $z = 0$ as baryons migrate into larger structures as part of cosmic structural growth. This means that most of the metals in the diffuse IGM at $z \sim 2$ are in galactic haloes at $z \sim 0$. Metals blown out from early galaxies to low overdensities are later reaccreted in the formation of larger structures, and blown out again. Still, the commonality of wind particles being recycled is surprising, especially since momentum-driven winds are almost always ejected at velocities well in excess of the escape velocity of the galaxy. It is in fact more appropriate to talk about how long it takes a wind particle to be recycled instead of whether it will be recycled. Metals injected by galactic superwinds cannot be assumed to remain permanently in the IGM; metals continuously cycle between galaxies and the IGM. In an upcoming paper, we will quantify the ages of metals observed at different absorption lines tracing different regions of the IGM. For now we note that the average ages of the metals in the IGM are typically much shorter than the age of the Universe.

Do wind particles generally return to their parent galaxy, or do they jump from galaxy to galaxy? The answer is the former; in the vast majority of cases a wind particle returns to either its parent galaxy or the result of a merger involving the parent galaxy. 95 per cent of recycled wind particles are re-launched from a galaxy of similar or more mass than the previous recycling. Of course galaxies grow anyway under the hierarchical growth scenario, so a wind particle could join a different galaxy that has itself grown larger than its parent. By considering wind particles recycled within 10 per cent of the Hubble time, we can diminish the bias of galaxy growth and explore whether winds are travelling from massive central galaxies to surrounding satellite galaxies possibly affecting their dynamics and enrichment histories. With this time limit, 97 per cent of winds return to more massive galaxies indicating that this is a less likely trend. The number jumps to 99 per cent when considering winds launched from $M_{\rm gal} > 10^{11}\,{\rm M}_{\odot}$, indicating that it is harder to escape from a more massive galaxy. Furthermore, a wind particle is rarely relaunched more than 1 comoving h^{-1} Mpc apart in a $16\,h^{-1}$ Mpc test simulation; the minority case usually involves wind particles following the position of a fast-moving parent galaxy. Winds rarely escape forever their parent halo, and winds from large central galaxies do not appear to disrupt satellite galaxies.

Another way to quantify wind recycling is using the summed amount of material injected into winds. We introduce the quantity $\Omega_{\rm wind}$, which is the mass injected in winds, including recycled gas. Owing to recycling, there is no limit to how large this can be. Using our l32n256 run, we find that $\Omega_{\rm wind} = 0.39\Omega_{\rm b}$ – that is, an equivalent of 39 per cent of the baryonic mass has been blown out in a galactic superwind by $z = 0$.[3] This is significantly larger than $\Omega_* = 0.097$ due to mass loading factors greater than 1 as well as recycling.

The other σ-derived wind runs to $z = 0$ give different values: $\Omega_{\rm wind} = 0.59\Omega_{\rm b}$ for the $8\,h^{-1}$ Mpc box with 128^3 SPH particles, and $\Omega_{\rm wind} = 0.23\Omega_{\rm b}$ for the $32\,h^{-1}$ Mpc box also with 128^3 particles. $\Omega_{\rm wind}$ increases by 160 per cent when mass resolution changes by 64 times. This jump is primarily due to a 70 per cent increase in Ω_*, but still leaves another 50 per cent likely due the varying treatment of recycling at different resolutions. This lack of resolution convergence raises the question of whether the amount of recycling is set by numerics, perhaps arising from the poor treatment of SPH trying to model outflow processes occurring at resolutions below the limit of our simulations.

The discontinuity in recycling rates between resolutions stems from how long and how far a particle reaches once it has been launched. Wind particles in the $32\,h^{-1}$ Mpc 2×256^3 box with typical masses of $3.2 \times 10^7\,{\rm M}_{\odot}$ are shot at hundreds of km s^{-1} – a huge bundle that may be more accurately thought of as a flying wind 'bullet'. An actual wind should form a bow shock resulting

[3] Although the total number of wind launches equals 45.7 per cent of all SPH particles, the typical wind particle is less massive than the average SPH particle, because one half of a full SPH particle remains when a star particle is spawned, and wind particles are more likely to arise from these remaining SPH particles.

Downloaded from https://academic.oup.com/mnras/article/387/2/577/1022513 by guest on 16 August 2022

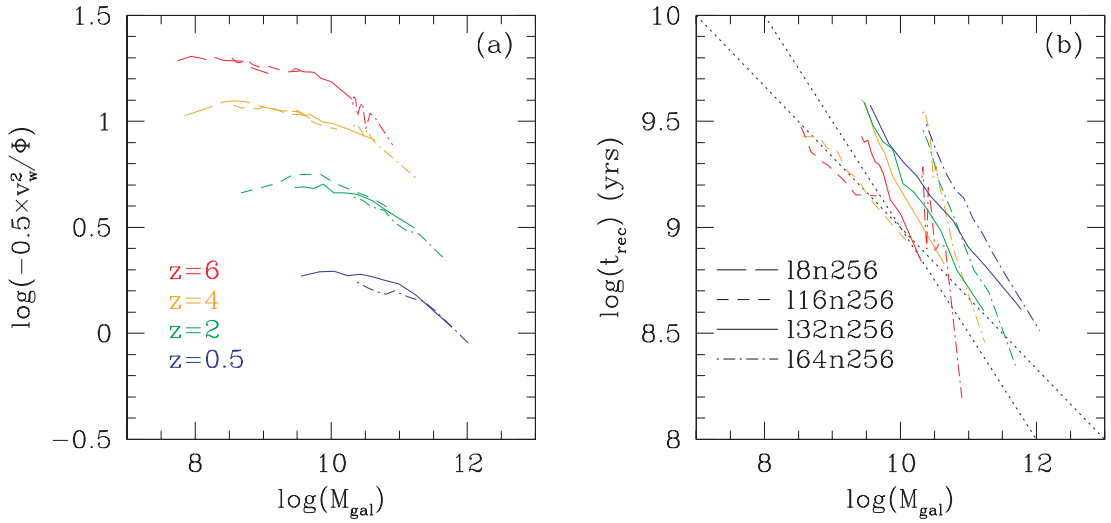

Figure 12. The virial ratio ($E_{\rm rat}$, the ratio of wind kinetic energy to potential well energy) are displayed as a function of galaxy mass (derived by SKID) at four launch redshifts in panel (a) for our σ-derived wind simulations at various box sizes. The shallow turnover at high-mass is mostly due to imposed wind speed limits. Panel (b) shows that the recycling time-scale (the median time for a wind particle to be relaunched in a wind) is a much stronger function of $M_{\rm gal}$. After exploring alternatives for the $M_{\rm gal}$–$t_{\rm rec}$ anticorrelation, we conclude that winds from more massive galaxies encounter a denser environment slowing the wind particle faster and allowing it to be re-accreted faster. The two dotted lines show that the galaxy mass dependence of $t_{\rm rec}$ is dominated by slowing due to environment, $M_{\rm gal}^{-1/3}$, or the gravitational free-fall time, $M_{\rm gal}^{-1/2}$; wind particles spend most of their time falling back into a galaxy. The poor resolution convergence in $t_{\rm rec}$ indicates that lower resolution simulations overpredict $t_{\rm rec}$ and underpredict the total amount of wind recycling. To see wind recycling in action in our simulations, see the movies and an explanation at http://luca.as.arizona.edu/∼oppen/IGM/recycling.html.

in a plume of material spreading laterally, but instead in SPH this speeding bullet is slowed down viscously through the interactions with neighbouring particles. The number of interacting neighbours over the same physical distance is lower at less resolution, and a wind particle will take longer to slow down; this is an unfortunate but unavoidable consequence of SPH. Hence, lower resolution simulations inhibit recycling as evidenced by the average number of times an individual wind particle is launched: 3.0, 2.5 and 2.1 times for 4.7, 38 and 300 $\times$ 10^6 $M_\odot$ SPH particle resolution (to $z = 0$). This lack of resolution convergence is quantifiable by the median recycling time-scale of wind particles in different resolution simulations as shown in the upper right-hand panel of Fig. 12, and is discussed in the following subsection. Increased resolution suggests that wind recycling should move $\Omega_{\rm wind}$ to an even higher value, probably exceeding $1/2\Omega_{\rm b}$. Given that galaxies below a certain mass cannot form owing to the presence of an ionizing background, there will be a limit to how high $\Omega_{\rm wind}$ can be; in the future we hope to run simulations that can achieve such resolutions in a cosmologically representative volume. For now, the wind recycling predictions should be considered as illustrative rather than quantitative.

5.4 Wind recycling time-scales

We now examine wind recycling as a function of galaxy mass. Specifically, we want to know what galaxies are able to inject their metals into the IGM. The common thought is that low-mass galaxies lose their metals more easily because winds can escape from these galaxies' shallower potential wells (e.g. Dekel & Silk 1986). As Dekel & Woo (2003) showed, if the outflow energy couples efficiently to ambient halo gas, this can yield the mass–metallicity relation as observed, as well as other properties of dwarf galaxies. However, Finlator & Davé (2008) showed that a model in which galaxies expel material at constant velocity (i.e. the 'constant wind' model of OD06) does not reproduce the observed mass–metallicity relation,primarily because outflows do not in fact couple their energy efficiently to ambient gas. Instead, the observed mass–metallicity relation (e.g. Tremonti et al. 2004; Erb et al. 2006) are better reproduced in the momentum-driven wind scenario. In this case, since $v_{\rm wind} \propto \sqrt{-\Phi_{\rm gal}}$ (roughly), all outflows have an approximately equal probability of escaping their parent haloes independent of mass, when considering only gravitational interactions with an isolated halo.

The left-hand panel of Fig. 12 shows the virial ratio, $E_{\rm rat} \equiv 0.5v_{\rm wind}^2/\Phi$, as a function of galaxy baryonic mass, for winds launched at four redshifts. At any given redshift, the ratio is roughly constant, but rises slightly at low masses and then declines to higher masses. At low masses, the trend arises from the mild metallicity dependence of $v_{\rm wind}$ together with the mass–metallicity relation. Moving to higher masses, since the potential Φ includes the galaxy potential and the environmental potential of the group/cluster in which it lies, and since massive galaxies live in denser environments, Φ is greater. At the highest masses, our imposed speed limit reflecting the assumption that wind energy cannot exceed twice the SN energy reduces wind velocities. Note that by definition, Φ-derived winds will have a constant $E_{\rm rat}$ for a given launch redshift (modulo wind speed limits); hence, the curvature towards high masses is predominantly a reflection of σ-derived winds.

In practice, outflows are not only confined by the gravitational potential of the host galaxy; cosmic infall and hydrodynamic effects can also be quite important. For instance, Ferrara, Scannapieco & Bergeron (2005) used a simulation of a typical LBG at $z = 3$ ($M_{\rm dyn} = 2 \times 10^{11}$ $M_\odot$) to show that metals never reach the IGM and instead are confined to the surrounding hot halo gas by infalling gas that creates a shock interface with the outflow.

One way to quantify such additional effects is to consider a new time-scale called the recycling time-scale, $t_{\rm rec}$, which is defined as the median time for a wind particle to be re-ejected again as a wind particle, or else fully converted into a star. At all launch redshifts

Downloaded from https://academic.oup.com/mnras/article/387/2/577/1022513 by guest on 16 August 2022

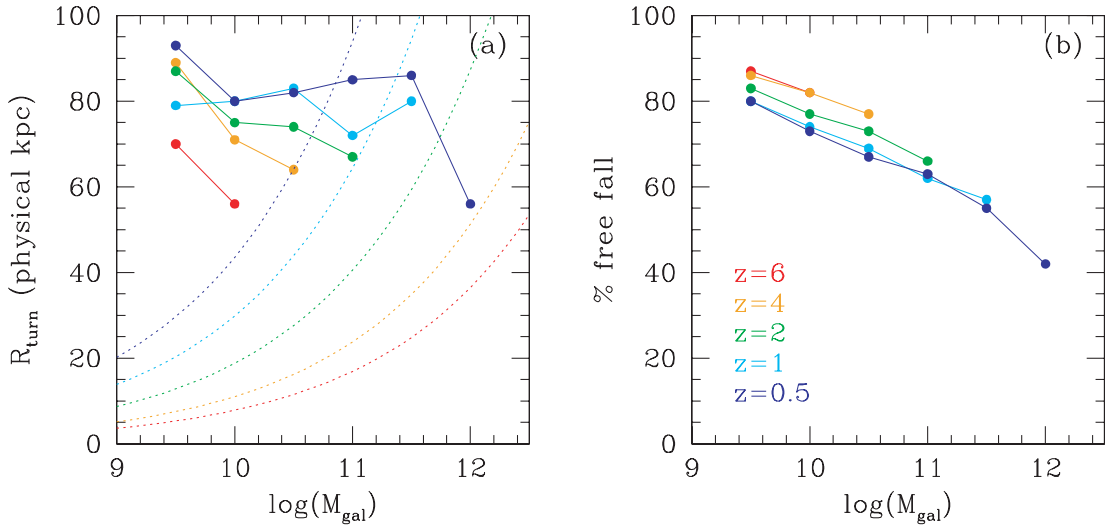

Figure 13. Panel (a) shows R_{turn}, the maximum radial extent a median wind particle may extend from its parent galaxy calculated from equation (9) in the l32n256 simulation. R_{turn} generally is larger at smaller M_{gal}; this trend coupled with the fact that t_{rec} is longer indicates that smaller galaxies can more easily enrich the IGM. Dotted lines corresponding to a NFW halo radius, r_{200} Navarro et al. (1997), show that winds from L^* galaxies do not escape their parent haloes at $z < 1$. Panel (b) shows that winds from small galaxies spend more time on their journey returning to a galaxy than being blown out.

explored, for all M_{gal}, more than half of wind particles recycle meaning that t_{rec} can be measured. The right-hand panel of Fig. 12 shows the t_{rec}–M_{gal} relation, demonstrating a strong anticorrelation of t_{rec} with galaxy mass. The simple fact that winds recycle on short time-scales even though they are launched at velocities well above the escape velocity is an indication that slowing by ambient gas and surrounding potentials is significant.[4]

If the galaxy's gravity is dominant in confining its outflow, one would expect that the time spent away from the galaxy would be approximated by twice the free-fall time-scale, t_{ff} (one t_{ff} outward and another one back in, or simply the orbital time-scale for an orbit of eccentricity 1). t_{ff} scales as $R_{turn}^{3/2}\ M_{dyn}^{-1/2}$, where R_{turn} is the turnaround distance of the wind particle, and M_{dyn} is the dynamical mass of the galaxy treated as a point source for the sake of simplicity. Following Newtonian dynamics, $R_{turn} \propto M_{dyn}/v_{wind}^2$, and the $v_{wind} \propto M_{gal}^{1/3}$ relation for momentum-driven winds, t_{ff} remains invariant as a function of galaxy mass while $R_{turn} \propto M^{1/3}$. Momentum-driven winds should reach a maximum distance from their parent galaxy that is a constant multiple of the virial radius since v_{wind} scales with the virial energy of an isolated halo. The strong trend of t_{rec} with M_{gal} indicates that larger scale potentials and hydrodynamic effects are dominant.

Is the particle spending more time in the IGM/galactic halo or in the galactic ISM before being relaunched? The answer is that the vast majority of the time between recycling is spent outside the star-forming regions of a galaxy. This is not surprising, because in our simulations the SF time-scale is tied completely to the accretion time-scale; once a particle is in a galaxy it gets converted to a star or blown out in a wind much more quickly than it was accreted (Finlator & Davé 2008). Therefore, we subdivide t_{rec} into two time-scales, one leaving the galaxy to reach R_{turn} while being slowed by hydrodynamical forces, t_{out}, and the other returning to the galaxy in approximately one t_{ff}. For simplicity, let us say that the hydrodynamic forces slow the wind particle down at a constant rate, in which case $t_{out} = R_{turn}/(v_{wind}/2)$. The total recycling time-scale can be approximated as

$$\frac{t_{rec}}{1\,\mathrm{Gyr}} = 1.96\left(\frac{R_{turn}}{100\,\mathrm{kpc}}\right)\left(\frac{100\,\mathrm{km\,s^{-1}}}{v_{wind}}\right) + 2.09\left(\frac{R_{turn}}{100\,\mathrm{kpc}}\right)^{3/2}\left(\frac{10^{10}\,\mathrm{M_\odot}}{M_{gal}}\right)^{1/2} \quad (9)$$

if we assume that $M_{dyn} = \Omega_M/\Omega_b \times M_{gal}$ and R_{turn} is in physical kpc. We can now solve for R_{turn} by taking the t_{rec} from Fig. 12 and the average v_{wind} from Fig. 3. R_{turn} is just an upper limit for how far wind particles with median t_{rec} can extend from a parent galaxy, because in reality a particle does not likely go out and then immediately fall back into a galaxy in two steps; wind particles often spend time orbiting around their parent galaxies as well.

In principle, R_{turn} can be tracked directly in simulations; however, our current suite of runs did not output position information of wind particles owing to the large storage requirements. We have checked for isolated cases that our simple formula (equation 9) yields roughly correct results.

We plot R_{turn} in the left-hand panel of Fig. 13, focusing first on the trend over 2.5 decades of galaxy masses at $z = 0.5$, which we consider here the local Universe since trends do not evolve much until $z = 0$. R_{turn} stays nearly constant from the size scale of dwarf galaxies to galaxies above L^* while t_{rec} declines. The dotted lines correspond to the radius, r_{200}, of a NFW halo (Navarro, Frenk & White 1997). The point at which R_{turn} and r_{200} intersect is the approximate transition mass below which winds reach the IGM and above which winds are confined to their haloes. Metals rarely enter the IGM from galaxies above $10^{11}\,\mathrm{M_\odot}$ in the local Universe. Several significant conclusions can be drawn from this behaviour at low z.

First let us consider our wind model and the Milky Way, which has $M_{gal} \sim 10^{11}\,\mathrm{M_\odot}$. Our wind model produces an outflow from a Milky Way type galaxy, with initial speeds of a few hundred km s^{-1}. One might claim that this immediately invalidates our model, since the

[4] For new movies showing wind recycling in action in our simulations, please visit http://luca.as.arizona.edu/~oppen/IGM/recycling.html.

Downloaded from https://academic.oup.com/mnras/article/387/2/577/1022513 by guest on 16 August 2022

Milky Way is not observed to have an outflow. Yet quantitatively, our model predicts that a Milky Way sized galaxy should have a recycling time of less than 1 Gyr, and the typical wind particle will not venture beyond 85 kpc (if we assume not much has changed between $z = 0.5 \rightarrow 0$). In other words, in our model, the Milky Way is not driving a classical outflow as seen from local starbursts, but rather is continually sending material up into the halo and having it to rain back down on a time-scale of 1 Gyr. We call this a *halo fountain*, in analogy with a galactic fountain that operates on smaller scales. Indeed, we speculate that there may not be a fundamental difference between galactic fountains and halo fountains, but rather gas is being thrown out of the disc at a range of velocities; however, our simulations lack the resolution to address this issue directly.

How might such a halo fountain be observed? One possibility is that it has already been seen, as HVCs. Wakker & van Woerden (1997) predict that, given the observed rate of material going into HVCs of about 5 $M_\odot$ yr^{-1}, then it should take ∼1 Gyr for all the gas in the ISM to cycle through this halo fountain. Hence, the Galaxy may have an active halo fountain recycling its material on a time-scale much less than a Hubble time, despite not resembling anything like a starburst galaxy. The difficulty of observation of feedback within our own Galaxy may just indicate how invisible yet ubiquitous galactic-scale winds are.

Secondly, with $R_{\rm turn}$ nearly constant, $t_{\rm rec}$ should be proportional to $M_{\rm gal}^{-1/3}$ if dominated by $t_{\rm out}$ and $M_{\rm gal}^{-1/2}$ if $t_{\rm ff}$ is larger. The black dotted line in the right-hand panel of Fig. 12 corresponding to the latter case (the steeper of the two) appears to more closely match the general trends indicating that $t_{\rm ff}$ dominates; wind particles spend a majority of $t_{\rm rec}$ falling into galaxies (panel b in Fig. 13). Our calculations above agree that $t_{\rm ff}$ grows larger than $t_{\rm out}$ for smaller galaxies, but the two time-scales are similar for extremely massive galaxies, $M_{\rm gal} \sim 10^{12}$ $M_\odot$.

Thirdly, smaller galaxies live in less dense environments where hydrodynamic slowing takes longer. To demonstrate this we look at another parameter, the minimum overdensity reached by wind particles, which should approximately correspond to the density at $R_{\rm turn}$. For the subset of wind particles, we track the minimum density achieved before recycling, $\rho_{\rm min}$. Fig. 14 (solid lines) shows the median $\rho_{\rm min}$ as a function of the baryonic mass of the originating galaxy, $M_{\rm gal}$, from the l32n256 run. At all redshifts, smaller galaxies push their winds to lower densities, consistent with them having longer recycling times. Their less dense environments slow winds over a longer $t_{\rm out}$, and allow them to reach a similar $R_{\rm turn}$ as more massive galaxies despite lower $v_{\rm wind}$. We also plot a long-dashed line that shows the average density within 1 comoving Mpc sphere around the $z = 0.5$ galaxies. These show a similar trend, indicating that environmental dependence is the primary factor in how far winds reach into the IGM and how long they remain there. The fact that $\rho_{\rm min}$ is much higher than the density within 1 Mpc is an indication that these winds are travelling much less than that distance as our calculations above indicate (∼80 kpc comoving at $z = 0.5$).

Although a possible explanation for the trend in $\rho_{\rm min}$ is that larger haloes have higher densities at the same distance, this cannot account for the dependence. The density of NFW haloes decline nearly as $1/r$ beyond r_{200} resulting in a $\rho_{\rm min} \propto M_{\rm gal}$ dependence much steeper than plotted in Fig. 14 below $z = 2$; for all but the most-massive galaxies the density contribution of the parent halo is much smaller at $\rho_{\rm min}$. The flattening of this relation towards $z = 0$ at $M_{\rm gal} < 10^{11}$ $M_\odot$ means these galaxies more likely live in denser environments. For more massive galaxies, the parent halo itself is more responsible for the hydrodynamical slowing.

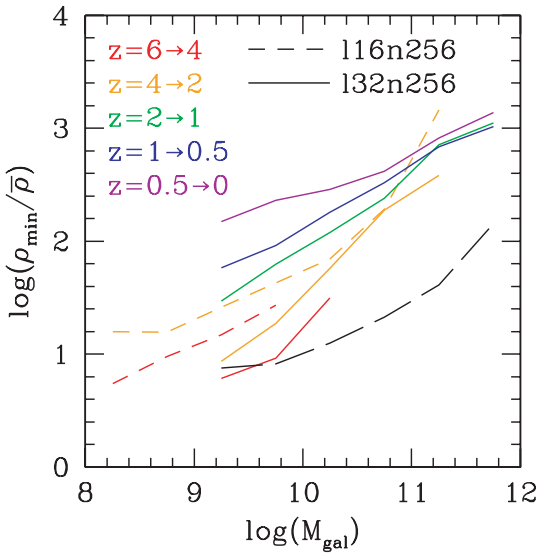

Figure 14. The minimum density a wind particle achieves between recyclings is shown to be a strong function of galaxy mass at all redshifts (coloured lines). Lower mass galaxies have longer recycling times, because winds are launched into less-dense environments where shocks take longer to slow and turn around winds. The environmental density within sphere of 1 comoving Mpc as a function of $M_{\rm gal}$ at $z = 0.5$ (black dashed line from l32n256 simulation) shows the same trend as $\rho_{\rm min}/\bar{\rho}$ indicating that environment is the primary factor in how far winds reach into the IGM. The NFW halo profile alone cannot explain this trend as halo profiles drop much more sharply and the environmental density dominates for all but the most-massive galaxies at low z.

Finally, small galaxies can enrich a similar volume as large galaxies leading to major implications as to which galaxies enrich the IGM. Metals from small galaxies have the advantage of staying in the IGM longer, however, the disadvantage of their winds being less metal enriched (e.g. panel b of Fig. 9). We plan to look at the origin of IGM metal absorbers in a future paper, exploring what galaxies enrich the IGM, how long these metals have been in the IGM, and what distance metals travel from their parent galaxy.

As a side note, we admit that the global SFRD is overestimated at late times ($z < 0.5$); the l32n256 run showing nearly four times as much SF at $z = 0$ relative to observations (Fig. 4). The primary reason for this discrepancy is the lack of a quenching mechanism in the largest galaxies; galaxies above 10^{11} $M_\odot$ account for 54 per cent of SF at $z = 0$, and their continued late growth creates far too many galaxies above this mass as compared to observations (Pérez-González et al. 2008). The influence of these overmassive galaxies on the IGM, however, appears to be remote due to their inability to inject metals beyond their haloes and their short recycling time-scales.

Turning to the evolution of recycling, $t_{\rm rec}$ grows moderately longer at lower redshift for a given $M_{\rm gal}$. For a 10^{10}-$M_\odot$ galaxy, $t_{\rm rec}$ is 1.1, 1.5, 1.6 and 2.0 Gyr for launch redshifts 6, 4, 2 and 0.5, respectively, in the $32\,h^{-1}$ Mpc box. This trend is in place despite $E_{\rm rat}$ declining by one decade from $z = 6 \rightarrow 0.5$ (see Fig. 12a); wind kinetic energy is declining relative to the potential at their launch location. Again, the overriding variable is the slowing of the wind by the environment; the average physical density declines by a factor of 100 in this interval, making it easier for winds to travel further despite a factor of 10 times less energy input into the winds. Galaxies of the same mass are more likely to live at higher overdensities at lower

Downloaded from https://academic.oup.com/mnras/article/387/2/577/1022513 by guest on 16 August 2022

redshift as structural growth makes more groups and clusters, but the declining physical densities and slower Hubble expansion of the Universe towards low redshift outweigh this.

While the $t_{\rm rec}$ grows at low redshift, the amount of the Universe it enriches sharply declines. The calculations of $R_{\rm turn}$ for equation (9) show a moderately increasing physical distance from $z = 6 \rightarrow 0.5$ with values of 56, 71, 75 and 80 kpc for the four respective launch redshifts when considering the same 10^{10}-$M_\odot$ galaxy. However, the comoving volume such a galaxy is enriching is $\{35\}$ times *greater* at $z = 6$ than at $z = 0.5$. Momentum-driven winds can more easily expel metals into the IGM at high redshift, whereas the overdense environments combined with weaker wind velocities and the overall larger scale of the Universe leave metals perpetually recycling in halo fountains in groups and clusters at low redshift. These are the *primary* reasons metals migrate from the IGM to galaxies as the Universe evolves.

Our results compare favourably to those of Bertone et al. (2007), who follow energy-driven winds ($\eta \propto \sigma^{-2}$ and $v_{\rm wind} \propto \sigma$) in their semi-analytical implementation using a two-phase process for the dynamical wind evolution (see also De Lucia & Blaizot 2007). At $z = 0$ they also find that it is the smaller galaxies ($10^{10.5} < M_{\rm dyn} < 10^{11.5}\,{\rm M}_\odot$, i.e. $\sim 1/10\,M^*$) that most efficiently inject their metals into the IGM ($\sim$40 per cent of the time), while metals from more massive haloes than $10^{12}\,{\rm M}_\odot$ rarely escape the halo and are recycled (see their fig. 9). This is despite their $v_{\rm wind}$ dependence (same as ours but without the scatter) exceeding the escape velocity. The redshift dependence is harder to compare to our results due to differing definitions of escaped fractions into the IGM, but they do also see smaller haloes, the progenitors to massive galaxies today, as the most efficient enrichers of the IGM up to $z = 4.5$.

Lastly, $t_{\rm rec}$ and $\rho_{\rm min}$ show similar resolution convergence issues as $\Omega_{\rm wind}$, for similar reasons. Lines at the same redshift do not overlap in either of these plots, indicating that $t_{\rm rec}$ is longer for the same $M_{\rm gal}$ at lower resolution. As discussed before, coarser resolution simulations slow down particles over a longer physical distance allowing wind particles to travel artificially too far at low resolution; this is why there is less recycling at lower resolution. For well-resolved galaxies, the lines of different resolution appear to nearly converge. The hydrodynamical treatment of wind particles after they are launched is not nearly as resolution-converged as the feedback properties on per galaxy basis (see Fig. 9). Recycling times are overestimated when underresolved. Hence, recycling times may actually be shorter than we've shown.

In summary, we have shown that wind recycling is an important phenomenon for understanding the evolution of galaxies and the IGM. Winds from galaxies are typically expelled and re-accreted on time-scales short compared to a Hubble time. This occurs despite the fact that winds are typically launched with plenty of kinetic energy to escape its halo. Such gravitational arguments are therefore not very relevant to understand how material cycles through galaxies and the IGM; instead, infall and shocks generated by outflows are more important in setting the wind distribution length- and time-scales. The recycling time is therefore strongly anticorrelated with galaxy mass, owing to the fact that more massive galaxies live in denser environments. These denser environments make it harder for winds to travel beyond their parent halo at late times causing the migration of metals from the IGM to galaxies from $z = 2 \rightarrow 0$. At the present epoch, small galaxies can still expel material, but larger galaxies are more aptly described as having halo fountains, in which material is constantly kicked up into the halo before raining down.

6 SUMMARY

We introduce a new version of GADGET-2, with improvements designed to explore mass, metal, and energy feedback from galactic outflows across all cosmic epochs. We add two major modules designed to make the code better suited to explore the low-z Universe: (1) a sophisticated enrichment model tracking four elements individually from Type II SNe, Type Ia SNe, and AGB stars; and (2) an on-the-fly galaxy finder used to derive momentum-driven wind parameters based on a galaxy's mass.

We first run test simulations to explore global energy and enrichment properties with and without AGB and Type Ia feedback, and with our old and new wind implementations. Focusing on our new (galaxy mass-derived) winds including all sources of feedback, we then run several 34 million-particle simulations to explore feedback over the history of the Universe and over a large dynamic range in galaxy mass. We also track a representative subset of wind particles to study in detail how mass, metals, and energy are distributed by outflows.

Our new chemical enrichment model enables us to investigate the global production and distribution of key individual metal species. Globally, metal production of all four species tracked (C, O, Si, Fe) is dominated by Type II SNe at all redshifts. Type Ia SNe add significantly to the iron content of hot, intracluster gas, especially at $z < 1$. AGB stars add moderately to the IGM carbon abundance by $z = 0$, and provide fresh (enriched) gas for recycling into stars which increases global SF at later epochs. Carbon yields from AGB stars cannot be ignored even at high z, because carbon AGB stars enrich on time-scales much less than a local Hubble time (i.e. 200 Myr–1 Gyr). Due to the complex interplay between instantaneous and delayed recycling from various forms, metallicity patterns in the IGM and ICM cannot be straightforwardly used to infer the enrichment patterns in the host galaxies responsible for polluting intergalactic gas.

We study enrichment patterns subdivided by baryonic phase. The total metal mass density is split roughly equally between galaxies and the IGM from $z = 6 \rightarrow 2$. Shocked intergalactic gas (WHIM and ICM) contains a fairly small portion of the global metal mass at all epochs. At $z < 2$, metals tend to migrate from the IGM into galaxies, so that by $z = 0$ about two-thirds of the metals are in galaxies (i.e. stars and cold gas). The combination of increased carbon and gas recycling from AGB feedback results in the IGM being significantly more carbon-enriched, which helps reproduce the relatively high observed mass density in C IV absorption systems at $z \approx 0$.

Our new galaxy mass based wind model implementation provides a more faithful representation of the momentum-driven wind model of MQT05, and yields outflows that are in better broad agreement with observed outflows. In particular, our implementation results in faster winds at high z and slower wind speeds at low z compared to our old local potential-derived winds. The fast early winds are able to enrich the IGM at early times as observed, while the slow late winds mean that most galaxies today are not driving material into the IGM at all. Qualitatively, this better agrees with observations indicating that most galaxies at $z \sim 2$–3 drive powerful winds (Erb et al. 2006), while today galaxies are rarely seen to have strong outflows.

We examine bulk properties of outflows as a function of galaxy mass. We find that mass, metallicity, and energy feedback as a function of galaxy baryonic mass roughly follow the trends predicted by momentum-driven winds: $\dot{M}_{\rm wind} \propto M_{\rm gal}^{2/3} H^{-1/3}(z)$ and $\dot{E}_{\rm wind} \propto M_{\rm gal}^{4/3} H^{1/3}(z)$. The metal outflow rate is $\dot{M}_{\rm wind} Z_{\rm gal}$, where $Z_{\rm gal} \propto M_{\rm gal}^{1/3}$ with a proportionality constant that increases with time

Downloaded from https://academic.oup.com/mnras/article/387/2/577/1022513 by guest on 16 August 2022

as given by mass–metallicity evolution (cf. Finlator & Davé 2008). The stellar mass of the typical (median) galaxy most responsible for each particular form of feedback increases by a factor of ∼30 between $z = 6 \rightarrow 2$, but only approximately 2–3 times from $z = 2 \rightarrow 0$. Each form of feedback traces a different mass scale: mass feedback $\sim \frac{1}{6}M^*$, energy feedback $\sim M^*$, and metallicity feedback $\sim \frac{1}{2}M^*$. Measuring these characteristic masses (e.g. B07) offers the possibility to test whether momentum-driven wind scalings are followed globally.

The wind energy relative to the SN energy scales roughly as $M_{\rm gal}^{1/3}$, and is within a factor of a few of unity at all epochs and galaxy masses. Given expected radiative losses from SN heat input into the ISM, it seems that SNe will have a difficult time providing enough energy to pollute the Universe as observed. An alternate source of energy would ease this tension, such as photons from young stars whose total energy can exceed the SN energy by several orders of magnitude. This adds to the circumstantial evidence supporting the idea that galactic outflows may be driven in large part by radiation pressure, as postulated in the momentum-driven wind model.

We find that *wind recycling*, material ejected as outflows and then re-accreted and ejected again, turns out to be a remarkably common occurrence with significant dynamical repercussions. By following individual wind particles in our simulations down to $z = 0$, we find that multiple recyclings are the norm, and that the typical wind particle has been ejected three to four times. In other words, outflow material being reaccreted on to a galaxy dominates over outflow material launched into the IGM forever. Since in our wind model all outflows are launched at speeds well above the escape velocity of galaxies, this indicates that outflows are mainly slowed through hydrodynamic interactions, allowing them to rejoin the hierarchical accretion flow into galaxies. Approximately, 20 per cent of the baryons participate in an outflow, but owing to multiple launchings the aggregate mass of baryons ejected exceeds half of the total baryonic mass. The two key corollaries of wind recycling as seen in our simulations are: (1) material driven in an outflow cannot be assumed to remain in the IGM forever, and (2) gravitational energetic considerations are generally not relevant for determining how far outflow propagate into the IGM.

We examine wind recycling as a function of galaxy mass. The recycling time scales roughly as $t_{\rm rec} \propto M_{\rm gal}^{-1/2}$, as expected if environmental effects are dominating the retardation of outflows. Larger galaxies have shorter recycling times despite launching winds at larger speeds, because they live in denser environments; the minimum overdensity achieved by winds scales with galaxy mass. As expected from the ubiquity of multiple recyclings, the recycling time is generally fairly short, roughly $10^{9\pm0.5}$ yr, increasing only mildly at lower redshift. Our analysis suggests that winds generally return to the galaxy from which they were launched (or its descendant), though a full merger tree construction is required to confirm this.

It is possible to estimate how far outflows travel from their host galaxies ($R_{\rm turn}$), as a function of galaxy mass and redshift. Remarkably, $R_{\rm turn} = 80 \pm 20$ *physical* kpc at all redshifts and masses. There are weak trends for higher $R_{\rm turn}$ at smaller masses and lower redshifts; both are consistent with ambient density being a key determinant for how far winds travel. The constant physical distance means that outflows at early epochs are able to enrich a significant fraction of the Universe, while outflows at later epochs are more confined around galaxies. This is the reason metals migrate from the IGM to galaxies between $z = 2 \rightarrow 0$.

Comparing $R_{\rm turn}$ to halo radii, we see that at $z > 2$, typical L^*-sized galaxies have outflows that escape their host halos into the IGM, while at $z < 1$ outflows are generally confined within galactic halos. This gives rise to the concept of *halo fountains*, where low-z galaxies are constantly kicking gas out of their ISM into the halo but no further, and this material rains back down on to the ISM on time-scales of order 1 Gyr or less. If correct, then even galaxies not canonically identified as having outflows (such as the Milky Way) may in fact be moving a significant amount of material around its halo. This halo fountain gas would be quite difficult to detect, as it is likely to be tenuous and multiphase; we broadly speculate that it might be responsible for HVCs or halo Mg II absorbers (e.g. Kacprzak et al. 2008). We leave a more thorough investigation of the observational consequences of halo fountains for the future.

As a final caveat, it should be pointed out that detailed properties of how outflows propagate out of galaxies are not as well converged with numerical resolution as we would like. This may be due to our particular way of implementing outflows in a Monte Carlo fashion combined with difficulties of SPH in handling individual outflowing particles. Here we have focused on qualitative trends that appear to be robust within our limited exploration of resolution convergence, without making overly detailed quantitative predictions. In the future, we plan to investigate how to implement outflows in a more robust way within the framework of cosmological hydrodynamic simulations.

Wind recycling and halo fountains provide two new twists on the idea of galactic outflows. If our models are correct, then there is a continuum of outflow properties from galactic fountains that barely kick gas out of the disc, to halo fountains that cycle material through gaseous halos of galaxies, to large-scale outflows that are for example, responsible for enriching the IGM. In short, outflows may be considerably more ubiquitous and complicated than previously thought, and hence understanding their effects on galaxies as a function of mass, environment, and epoch will be even more critical for developing a comprehensive model for how galaxies form and evolve.

ACKNOWLEDGMENTS

We thank J. Bieging, N. Bouché, M. Fardal, K. Finlator, N. Katz and R. Somerville for useful conversations and inspiring new avenues of exploration. We thank V. Springel for contributing his FOF finder, which we later modified for use in our simulations. The simulations were run on the Xeon Linux Supercluster at the National Centre for Supercomputing Applications, the University of Arizona's 512-processor SGI Altix system housed at the Centre for Computing & Information Technology, and our 16-processor Opteron systems. The authors thank H.-W. Rix and the Max-Planck-Institüt für Astronomie for their gracious hospitality while some of this work was being done. Support for this work, part of the Spitzer Space Telescope Theoretical Research Program, was provided by NASA through a contract issued by the Jet Propulsion Laboratory, California Institute of Technology under a contract with NASA. Support for this work was also provided by NASA through grant number HST-AR-10946 from the Space Telescope Science Institute, which is operated by AURA, Inc., under NASA contract NAS5-26555.

REFERENCES

Aguirre A., Hernquist L., Schaye J., Weinberg D. H., Katz N., Gardner J., 2001, ApJ, 560, 599
Anders E., Grevesse N., 1989, Geochim. Cosmochim. Acta, 53, 197
Balogh M. L., Pearce F. R., Bower R. G., Kay S. T., 2001, MNRAS, 326, 1228
Bell E. F., McIntosh D. H., Katz N., Weinberg M. D., 2003, ApJS, 149, 289

© 2008 The Authors. Journal compilation © 2008 RAS, MNRAS **387,** 577–600

Downloaded from https://academic.oup.com/mnras/article/387/2/577/1022513 by guest on 16 August 2022

Bertone S., De Lucia G., Thomas P. A., 2007, MNRAS, 379, 1143
Boksenberg A., Sargent W. L. W., Rauch M., 2003, in Perez E., Delgado R. M. G., Tenorio-Tagle G., eds, ASP Conference Proceedings, Vol. 297, 447, (BSR03)
Bouché N., Lehnert M. D., Aguirre A., Péroux C., Bergeron J., 2007, MNRAS, 378, 525 (B07)
Bouwens R. J., Illingworth G. D., Franx M., Ford H., 2007, ApJ, 670, 928
Bressan A., Fagotto F., Bertelli G., Chiosi C., 1993, A&AS, 100, 647
Bruzual G., Charlot S., 2003, MNRAS, 344, 1000
Caputi K. I. et al., 2006, ApJ, 637, 727
Cattaneo A. et al., 2007, MNRAS, 377, 63
Cen R., Fang T., 2006, ApJ, 650, 573
Cen R., Ostriker J. P., 1999, ApJ, 514, 1
Cen R., Ostriker J. P., 2006, ApJ, 650, 560
Cen R., Tripp T. M., Ostriker J. P., Jenkins E. B., 2001, ApJ, 559, L5
Chabrier G., 2003, PASP, 115, 763
Chen X., Weinberg D. H., Katz N., Davé R., 2003, ApJ, 594, 42
Cole S. et al., 2001, MNRAS, 326, 255
Cowie L. L., Songaila A., 1998, Nat, 394, 44
Dalla Vecchia C., Schaye J., 2008, MNRAS, in press (arXiv:0801.2770)
Davé R., 2008, MNRAS, 385, 147
Davé R., Oppenheimer B. D., 2007, MNRAS, 374, 427 (DO07)
Davé R., Hernquist L., Katz N., Weinberg D. H., 1999, ApJ, 511, 521
Davé R., Finlator K., Oppenheimer B. D., 2006, MNRAS, 370, 273
De Lucia G., Blaizot J., 2007, MNRAS, 375, 2
Dekel A., Birnboim Y., 2006, MNRAS, 368, 2
Dekel A., Silk J., 1986, ApJ, 303, 39
Dekel A., Woo J., 2003, MNRAS, 344, 1131
Di Matteo T., Springel V., Hernquist L., 2005, Nat, 433, 604
Erb D. K., Shapley A. E., Pettini M., Steidel C. C., Reddy N. A., Adelberger K. L., 2006, ApJ, 644, 813
Evrard A. E. et al., 2008, ApJ, 672, 122
Fardal M. A., Katz N., Weinberg D. H., Davé R., 2007, MNRAS, 379, 985.
Ferrara A., Scannapieco E., Bergeron J., 2005, ApJ, 634, L37
Finlator K., Davé R., 2008, MNRAS, 385, 2181
Finlator K., Davé R., Papovich C., Hernquist L., 2006, ApJ, 639, 672
Finlator K., Davé R., Oppenheimer B. D., 2007, MNRAS, 376, 1861
Fontana A. et al., 2006, A&A, 459, 745
Frye B. L., Tripp T. M., Bowen D. B., Jenkins E. B., Sembach K. R., 2003, in Rosenberg J. L., Putman M. E., eds, ASSL Conf. Proc. Vol. 281, The IGM/Galaxy Connection: The Distribution of Baryons at z=0. Kluwer, Dordrecht, p. 231
Fujita A., Mac Low M.-M., Ferrara A., Meiksin A., 2004, ApJ, 613, 159
Fujita A., Martin C. L., Mac Low M.-M., New K. C. B., Weaver R. 2008, ApJ, submitted (arXiv:0803.2892)
Fukigita M., Peebles P. J. E., 2004, ApJ, 616, 643
Gavilán M., Buell J. F., Mollá M., 2005, A&A, 432, 861
Helsdon S. F., Ponman T. J., 2000, MNRAS, 315, 356
Herwig F., 2004, ApJS, 155, 651
Hirschi R., Meynet G., Maeder A., 2005, A&A, 433, 1013
Hopkins A. M., Beacom J. F., 2006, ApJ, 651, 142
Kacprzak G. G., Churchill C. W., Steidel C. C., Murphy M. T., 2008, AJ, 135, 922
Kennicutt R. C., 1998, ApJ, 498, 541
Kereš D., Katz N., Weinberg D. H., Davé R., 2005, MNRAS, 363, 2
Kobayashi C., 2004, MNRAS, 347, 740
Kobayashi C., Springel V., White S. D. M., 2007, MNRAS, 376, 1465
Lia C., Portinari L., Carraro G., 2002, MNRAS, 330, 821
Lilly S. J., Le Fevre O., Hammer F., Crampton D., 1996, ApJ, 460, L1
Limongi M., Chieffi A., 2005, in Turatto M., Benetti S., Zampieri L., Shea W., eds, ASP Conf. Ser. Vol. 342, 1604-2004: Supernovae as Cosmological Lighthouses. Astron. Soc. Pac., San Francisco, p. 122
McKee C. F., Ostriker J. P., 1977, ApJ, 218, 148
Mac Low M.-M., Ferrara A., 1999, ApJ, 513, 142
Madau P., Ferguson H. C., Dickinson M. E., Giavalisco M., Steidel C. C., Fruchter A., 1996, MNRAS, 283, 1388
Mannucci F., Della Valle M., Panagia N., Cappellaro E., Cresci G., Maiolino R., Petrosian A., Turatto M., 2005, A&A, 433, 807
Marigo P., 2001, A&A, 370, 194
Martin C. L., 2005a, ApJ, 621, 227
Martin C. L., 2005b, in Brown R., ed., ASP Conf. Ser. Vol. 331, Extra-Planar Gas. Astron. Soc. Pac., San Francisco, p. 305
Mo H. J., Mau S., White S. D. M., 1998, MNRAS, 295, 319
Mulchaey J. S., 2000, ARA&A, 38, 289
Murray N., Quatert E., Thompson T. A., 2005, ApJ, 618, 569 (MQT05)
Navarro J. F., Frenk C. S., White S. D. M., 1997, ApJ, 490, 493
Oppenheimer B. D., Davé R. A., 2006, MNRAS, 373, 1265 (OD06)
Papovich C. et al., 2006, ApJ, 640, 92
Pérez-González P. G. et al., 2005, ApJ, 630, 82
Pérez-González P. G. et al., 2008, ApJ, 675, 234
Pettini M., Shapley A. E., Steidel C. C., Cuby J.-G., Dickinson M., Moorwood A. F. M., Adelberger K. L., Giavalisco M., 2001, ApJ, 554, 981
Pettini M., Madau P., Bolte M., Prochaska J. X., Ellison S. L., Fan X., 2003, ApJ, 594, 695
Portinari L., Chiosi C., Bressan A., 1998, A&A, 334 505
Renzini A., Voli M., 1981, A&A, 94, 175
Rozo E. et al., 2007, ApJ, submitted (astro-ph/0703571)
Rupke D. S., Veilleux S., Sanders D. B., 2005, ApJS, 160, 115
Ryan-Weber E. V., Pettini M., Madau P., 2006, MNRAS, 371, L78
Salpeter E. E., 1955, ApJ, 121, 161
Scannapieco E., Bildsten L., 2005, ApJ, 629, L85
Schaerer D., 2003, A&A, 397, 527
Shapley A. E., Steidel C. C., Pettini M., Adelberger K. L., 2003, ApJ, 588, 65
Simcoe R. A., 2006, ApJ, 653, 977
Sommer-Larsen J., Fynbo J. P. U., 2008, MNRAS, 385, 3
Songaila A., 2001, ApJ, 561, L153
Songaila A., 2005, AJ, 130, 1996
Spergel D. N. et al., 2007, ApJS, 170, 377
Spitoni E., Recchi S., Matteucci F., 2008, A&A, in press (arXiv:0803.3032)
Springel V., 2005, MNRAS, 364, 1105
Springel V., Hernquist L., 2002, MNRAS, 333, 649
Springel V., Hernquist L., 2003a, MNRAS, 339, 289 (SH03a)
Springel V., Hernquist L., 2003b, MNRAS, 339, 312 (SH03b)
Strickland D. K., Heckman T. M., Weaver K. A., Hoopes C. G., Dahlem M., 2002, ApJ, 568, 689
Swinbank A. M., Bower R. G., Smith G. P., Wilman R. J., Smail I., Ellis R. S., Morris S. L., Kneib J.-P., 2007, MNRAS, 376, 479
Thielemann F.-K., Nomoto K., Yokoi K., 1986, A&A, 158, 17
Tremonti C. A. et al., 2004, ApJ, 613, 898
Tremonti C. A., Moustakas J., Diamond-Stanic A. M., 2007, ApJ, 663, L77
Trujillo I. et al., 2006, MNRAS, 373, L36
Trujillo I., Conselice C. J., Bundy K., Cooper M. C., Eisenhardt P., Ellis R. S., 2007, MNRAS, 382, 109
Tsujimoto T., Nomoto K., Yoshii Y., Hashimoto M., Yanagida S., Thielemann F.-K., 1995, MNRAS, 277, 945
Twarog B. A., 1980, ApJ, 242, 242
Wakker B. P., van Woerden H., 1997, ARA&A, 35, 217
Wallerstein G., Knapp G. R., 1998, ARA&A, 36, 369
Wilman R. J., Gerssen J., Bower R. G., Morris S. L., Bacon R., de Zeeuw P. T., Davies R. L., 2005, Nat, 436, 227
Woosley S. E., Weaver T. A., 1995, ApJS, 101, 181

This paper has been typeset from a TEX/LATEX file prepared by the author.

Downloaded from https://academic.oup.com/mnras/article/387/2/577/1022513 by guest on 16 August 2022